







Study of star formation in dual nuclei galaxies using UVIT observations

K. Rubinur ^{1,2}★, M. Das ³, P. Kharb ², J. Yadav ^{3,4}, C. Mondal ⁵ and P.T. Rahna ^{6,7}

¹*Institute of Theoretical Astrophysics, University of Oslo, PO box 1029 Blindern, Oslo 0315, Norway*

²*National Centre for Radio Astrophysics-Tata Institute of Fundamental Research (NCRA-TIFR), S. P. Pune University Campus, Ganeshkhind, Pune 411007, India*

³*Indian Institute of Astrophysics, Koramangala II Block, Bangalore 560034, India*

⁴*Pondicherry University, R.V. Nagar, Kalapet, Puducherry 605014, India*

⁵*Inter-University Centre for Astronomy and Astrophysics, Ganeshkhind, Post Bag 4, Pune 411007, India*

⁶*CAS Key Laboratory for Research in Galaxies and Cosmology, Shanghai Astronomical Observatory, Shanghai 200030, China*

⁷*Centro de Estudios de Física del Cosmos de Aragón (CEFCA), Plaza San Juan 1, E-44001 Teruel, Spain*

Accepted 2024 January 29. Received 2024 January 23; in original form 2023 January 1

ABSTRACT

We have used the Ultraviolet Imaging Telescope (UVIT) aboard AstroSat to study star formation in a sample of nine dual nuclei galaxies with separations $\lesssim 11$ kpc, which is an expected outcome of galaxy mergers. To minimize the contribution of active galactic nuclei (AGN) emission, we have used mid-IR colour cut-offs and masked the AGN-dominated nuclei. The UV continuum slope (β) is used to calculate the internal extinction (A_V) which ranges from 0.53 to 4.04 in the FUV band and 0.44 to 3.10 in the NUV band for the sample. We have detected 1–20 star-forming clumps in our sample galaxies. The extinction-corrected total FUV star formation rate (SFR) ranges from ~ 0.35 to $\sim 32 M_{\odot} \text{ yr}^{-1}$. Our analyses of A_V , specific SFR (sSFR) show that dual nuclei sources are associated with dusty, star-forming galaxies. The FUV – NUV colour maps show redder colour in the nuclear and disc regions while bluer colour is observed in the outskirts of most galaxies which can be due to embedded dust or different stellar populations. We have found some signatures of possible stellar/AGN feedback like a ring of star formation, a redder ring around blue nuclei, etc. However, further observations are required to confirm this.

Key words: galaxies: active – galaxies: formation – galaxies: star formation – radio continuum: galaxies – ultraviolet: galaxies.

1 INTRODUCTION

Galaxies show a bimodality in the star formation rate (SFR)–stellar mass (M_{\star}) plane. It has been found that while early-type galaxies, which are mostly elliptical and S0 galaxies with old stellar populations, form the red cloud, the late-type spiral galaxies, which are star-forming, occupy the blue cloud. The green valley is defined as the region of transition between early-type and late-type galaxies (Daddi et al. 2007; Salim et al. 2007; Elbaz et al. 2018). Statistically large samples of early-type galaxies show that most of the stellar mass has been accumulated in the past 8 billion years (Brown et al. 2007). There are several processes that can help to build the stellar mass: one of the most important being galaxy mergers (Hopkins & Quataert 2010).

Hierarchical galaxy formation theories predict that galaxies have formed through several major (mass ratio $\geq 1:3$) and minor (mass ratio $\leq 1:3$) mergers (Volonteri, Haardt & Madau 2003; Springel 2005). Two spiral galaxies can form an elliptical galaxy through a major merger and it can turn into a starburst galaxy depending on the availability of gas. Hence, galaxy mergers are the key drivers of galaxy evolution (e.g. Barnes & Hernquist 1992), and understanding these systems is important. The tidal forces due to

the interaction produce non-axisymmetric gravitational forces across the discs causing enormous changes in the potential of the galaxies (Bournaud 2010). These changes cause an increase in cloud collisions and shocks resulting in star formation (SF) (e.g. Kennicutt Robert et al. 1987; Saitoh et al. 2009; Ellison et al. 2013). Therefore, mergers can disturb the galaxies leading to gas inflow towards the galaxy nuclei as well as within the parent galaxies, often leading to starburst activity in the galaxies (Hopkins & Hernquist 2009). Observations of such merger-induced SF suggest that most galaxy mergers should go through the starburst phase (Schweizer 2005). However, recent observations show that such starburst activity is found only in a minority of galaxy mergers. On the other hand, simulations of merging galaxies have shown that SFR is increased when galaxies are close to each other during the first, second pericenter passes, and finally during coalescence (e.g. Hopkins et al. 2006; Rupke, Kewley & Barnes 2010). However, in between these periods of close separation, which forms most of the interaction time, the SFR increases at most by a factor of two which is much lower than the SFRs expected from starburst galaxies (Moreno et al. 2019).

Several studies have tried to understand the effect of mergers at different galaxy separations, different redshifts, and with different types of galaxies (Ellison et al. 2013; Knapen, Cisternas & Querejeta 2015). Major mergers can grow 20 per cent of the mass for massive galaxies in $z < 1$ which is significant but not sufficient (López-Sanjuan et al. 2010). This leads to the requirement of minor mergers

* E-mail: rubi.khatun35@gmail.com

for galaxy growth. It has been found that minor mergers contribute to almost ~ 35 per cent of the SF over the cosmic time (Kaviraj 2014). Hence, both major and minor mergers are important to understand the galaxy evolution in terms of SF and nuclear activity.

SF can be studied using UV and H α observations (e.g. Kennicutt 1998; Calzetti 2013). The H α arises from massive O- and B-type stars. The lifetime of these stars is only $\sim 10^6$ – 10^7 yr; therefore, H α effectively traces SF only for a short period. On the other hand, UV emission arises from the ionizing radiation of O-, B-, and A-type stars, as well as some evolved stars, so it traces SF for $\sim 10^6$ – 10^8 yr, i.e. 10 times longer than H α . A part of UV emission in the galaxies is absorbed by the dust within the galaxy and is re-emitted in the infrared (IR). One needs to correct the UV emission for dust extinction to calculate the total SFR.

The gas inflow (Hopkins & Hernquist 2009) towards the centres during the merger can ignite the accretion activity to the central supermassive black hole and turn them into active galactic nuclei (AGN) (mass $\sim 10^6$ – $10^8 M_{\odot}$; Mihos & Hernquist 1996; Mayer et al. 2007). Studies have found that the AGN fraction increases with the number of mergers (Ellison et al. 2011). Once AGN activity is triggered and the SMBHs reach a certain critical mass (Ishibashi & Fabian 2012), they give out energy to the surrounding medium via winds, jets, and radiation. The winds can trigger SF beyond the AGN by shocking gas; the outflowing winds can also suppress gas infall due to the pressure of the gas and the radiation. This is collectively called AGN feedback (see Fabian 2012; Harrison 2017; Morganti 2017, for review). In the low-mass starburst galaxies, stellar-driven galactic winds are also significant (see Zhang 2018, for review). Stellar-driven feedback can work together with AGN feedback in some galaxies (Rupke & Veilleux 2011). Theories show that during mergers, after an intense burst of SF and black hole accretion, the feedback processes can remove the gas as well as heat the interstellar medium (ISM) which prevents gas cooling. This process can suppress the SF and transform blue galaxies into red galaxies in SFR– M_* plane (Hopkins et al. 2008; Ellison et al. 2022, and reference therein).

The whole process of SFs, and AGN activity during mergers is not yet well understood, especially in dual nuclei galaxies which are one of the outcomes of galaxy mergers. Many dual nuclei galaxies are found in the surveys of interacting galaxies such as ultraluminous infrared galaxies (ULIRGs; Mazzarella, Bothun & Boroson 1991). Mazzarella et al. (1988, 2012) have studied individual systems using multiwavelength observations. Some studies approach dual nuclei galaxies from the merger hypothesis angle (Gimeno, Díaz & Carranza 2004; Mezcuca et al. 2014) while others focus on the nuclear emission to detect AGN pairs (or dual AGN) (Koss et al. 2012; Rubinur et al. 2021). Thus, dual nuclei galaxies can help us to investigate the final stages of galaxy mergers.

So far, most of the studies in the literature have explored SF in galaxies as well as galaxy pairs or mergers using *GALEX*.¹ UV observations which has an angular resolution of ~ 5 arcsec (e.g. Smith et al. 2010; Yuan et al. 2012). However, the Ultraviolet imaging telescope (UVIT) (Kumar et al. 2012) onboard ASTROSAT, has a better angular resolution of ~ 1.2 arcsec. Several nearby galaxies have been explored which have produced better-resolution images. Some examples of such studies are star-forming clumps (SFCs) in extended ultraviolet (XUV) disc galaxies (e.g. Das et al. 2021; Yadav et al. 2021b), dwarf galaxies (e.g. Mondal, Subramaniam & George 2018), spiral galaxies (e.g. Rahna et al. 2018), post-merger galaxies (e.g. George et al. 2018a,b; Yadav et al. 2023).

In this paper, we have studied the SF in a sample of UV-bright dual nuclei galaxies using UVIT observations. The paper is structured as follows: The sample selection is discussed in Section 2. Section 3 describes the UVIT observations, details of archival IR data, and data analysis. Further image analysis and estimation of required parameters like extinction, SFR, and M_* are discussed in Section 4. The results are presented in Section 5 along with the discussions. The summary and conclusion are given in Section 6. We have used the cosmology with $\Omega_m = 0.27$ and $H_0 = 73.0 \text{ km s}^{-1} \text{ Mpc}^{-1}$. The spectral index, α , is defined such that the flux density at frequency ν is $S_{\alpha} \propto \nu^{\alpha}$.

2 SAMPLE SELECTION

We started this as a pilot study to explore SF in dual nuclei galaxies with UVIT. Here, we define dual nuclei as those with a projected separation of ~ 10 kpc and we include nuclei of all types, i.e. both AGN and SF types. Our main criterion is that the nuclei should be embedded in one common envelope or closely interacting. For the UVIT observations, the sample had to go through several instrument/UV criteria such as (a) galaxies with strong UV detection in previous UV surveys such as in *GALEX*², (b) the sources must be visible in the sky (tool *Astrovviewer*³), (c) there should not be any bright source in the field which could harm the telescopes (tool *BSWT*⁴). We started from an initial sample of merger systems from Mezcuca et al. (2011); they carried out a photometric study of a sample of 52 dual nuclei systems. We selected six systems from their study. To increase the sample, we included one sample galaxy from Ge et al. (2012) and two sample galaxies from Liu et al. (2011), both of which are studies of narrow emission-line galaxies with double-peaked AGN that are dual AGN candidates (Rubinur, Das & Kharb 2019). Along with these nine sources, we have included another source ESO509–IG006 which is a closely interacting galaxy pair with a separation of ~ 11 kpc (Guainazzi et al. 2005). Our final sample had 10 dual nuclei galaxies. One of these galaxies (MRK 212) is presented in Rubinur et al. (2021), where two SF knots near one of the nuclei are detected in the 15 ksec UVIT image. Hence, the rest of the nine galaxies (Table 1) are presented in this work.

3 OBSERVATIONS AND DATA REDUCTION

3.1 Ultraviolet

Our primary motivation in this study is to understand global SF in galaxies as well as local SF traced by the SFCs using high-resolution UV images. The main instrument used in this study is the UVIT, which is one of the five payloads onboard India’s first Astronomical satellite AstroSat (Kumar et al. 2012). The UVIT consists of two co-aligned Ritchey Chretien UV telescopes with a field of view of 28 arcmin. One telescope is assigned for FUV observations (1300–1800 Å) and the other one for the NUV (2000–3000 Å) and optical bands. The expected spatial resolution of the telescopes is ~ 1.2 – 1.5 arcsec, which is more than three times better than *GALEX* (~ 5 arcsec). The individual bands have multiple filters with different bandwidths.

We obtained UVIT data for nine of these galaxies in the initial cycles (A02–A04). After inspection of the initial short exposure

¹<http://www.galex.caltech.edu/>

²<https://galex.stsci.edu/GR6/?page=mastform>

³<http://issdc.gov.in/astroviewer/index.html>

⁴<https://uvit.iap.res.in/Software/bswt>

Table 1. Details of sample dual nuclei galaxies

No	Object	RA (J2000)	Dec. (J2000)	Redshift	Distance (Mpc)	Scale (kpc arcsec ⁻¹)	Nuclei 1 Type (8)	Nuclei 2 Type (9)	Separation (arcsec)	Separation (Kpc)	Reference
(1)	(2)	(3)	(4)	(5)	(6)	(7)	(8)	(9)	(10)	(11)	(12)
1	MRK 306	22 ^h 31 ^m 51 ^s .2	+19°41'9"	0.018 696	72.9	0.341	Starburst	Unknown	4.8	1.6	Mezcua et al. (2014)
2	MRK 721	10 ^h 23 ^m 32 ^s .6	+10°57'35"	0.032 092	140	0.636	Starburst	Unknown	5.4	3.4	Mezcua et al. (2014)
3	MRK 789	13 ^h 32 ^m 24 ^s .2	+11°06'23"	0.031 454	137	0.621	AGN	Unknown	4.7	2.9	Mezcua et al. (2014)
4	NGC 3773	11 ^h 38 ^m 12 ^s .9	+12°06'43"	0.003 276	18.3	0.088	Starburst	Unknown	3.2	0.3	Mezcua et al. (2014)
5	MRK 739	11 ^h 36 ^m 29 ^s .1	+21°35'46"	0.029 854	130	0.594	AGN	AGN	6.2	3.7	Mezcua et al. (2014)
6	ESO509-IG066	13 ^h 34 ^m 40 ^s .8	-23°26'45"	0.033 223	144	0.654	AGN	AGN	16	10.9	Guainazzi et al. (2005)
7	SDSS J143648.10+182037.6	14 ^h 36 ^m 48 ^s .1	+18°20'38"	0.049 421	214	0.940	Starburst	Unknown	5.5	5.2	Ge et al. (2012)
8	SDSS J101920.83+490701.2	10 ^h 19 ^m 20 ^s .8	+49°07'01"	0.054 087	235	1.022	AGN	AGN	4.6	4.9	Liu et al. (2011)
9	SDSS J102700.40+174901.0	10 ^h 27 ^m 00 ^s .4	+17°49'01"	0.066 619	293	1.245	AGN	COMP	2.4	3.0	Liu et al. (2011)

Notes. Column 2: full name of the sample galaxies. Later on, shorter versions are used. Columns 3 and 4: RA (right ascension) and Dec. (declination) in the J2000 epoch. Columns 5 and 6: redshift (z) and distance. Column 7: Scale of the systems. Columns 8 and 9: nature of the nuclei. Columns 10 and 11: separations of the nuclei in arcsec and kpc scales. Column 12: references.

(1–5 ksec) observations, we obtained deep observations (≥ 6 ksec) for two of these galaxies in cycle A07 (Table 2). The initial observations were carried out with both the NUV and FUV filters (A02–165 and A03–091). However, the NUV channel stopped working since A04. So, here we present UVIT observations of nine dual nuclei galaxies where eight have both FUV and NUV band data while one object has only FUV data. We have used *GALEX* images and magnitudes wherever needed. The details of the observations are given in Table 2.

The level 1 UVIT data of the sample galaxies were downloaded from the Indian Space Science Data Centre (ISSDC). A graphical user interface CCDLAB (Postma & Leahy 2017) was used to reduce the level 1 data. The CCDLAB does the field distortion and drift corrections. Astrometry for all the sources was done using the GAIA data set. A tool in CCDLAB matches sources from GAIA catalogue (Gaia Collaboration et al. 2023) with UVIT sources and applies astrometric corrections.

3.2 Infrared

The mid-IR (MIR) colour–colour plot (Fig. 1) is a good tool to understand the AGN dominance in galaxy emission. Also, the MIR colour can be used to calculate the stellar mass of the galaxies (Cluver et al. 2014). In our study, we have used data from the *Wide-field Infrared Survey Explorer* (*WISE*; Wright et al. 2010). *WISE* mapped the entire sky at four MIR filters centred at $W1$: 3.4 μm , $W2$: 4.6 μm , $W3$: 12 μm , and $W4$: 22 μm . The photometry magnitudes are taken from IRSA page⁵ and used for further analysis.

4 ANALYSIS

In this section, we discuss the steps taken for further UV image analysis as well as calculating the extinction, SFR, and stellar masses.

4.1 AGN dominance and masking

Five out of the nine galaxies have confirmed AGN (or multiple AGN) (Table 1). It is therefore important to understand the contribution of AGN activity to the galaxy UV emission. The AGN spectra are expected to be redder than the non-active galaxy spectra in the 1–10- μm range. Hence, the AGN host galaxies have a different location in the MIR colour–colour diagram. Several cut-offs are used to segregate the AGN emission (Stern et al. 2005; Jarrett et al. 2011). We have used a standard diagnostic *WISE* colour–colour ($W2 - W3$ versus $W1 - W2$) diagram (Fig. 1) to understand if our sample galaxies have any dominant AGN emission or not, using cut-offs from Stern et al. (2012) and Blecha et al. (2018). We found that only MRK 739 and the western galaxy of the ESO 509-IG066 system are above the $W1 - W2$ cutoff of 0.5. As the AGN is not resolved in our images, we have created an aperture with \sim PSF size with a radius of ~ 3 pixels and then masked both the nuclei of MRK 739 and the western nucleus of ESO 509-IG066 using *photutils* library in PYTHON. Later on, we also masked the nuclei of SDSS J101920.83+490701.2 (see Section 5.1). It is possible that the nuclei of other two galaxies with AGN (e.g. MRK 789 or SDSS J102700.40+174901.0) have contributed to the UV emission. However, those are not AGN dominant and the nuclei are not resolved enough to perform the mask analysis.

Apart from AGN nuclei masking, we have used this technique on the following galaxies (i) MRK 306: The companion galaxy MRK

⁵<https://irsa.ipac.caltech.edu/frontpage/>

Table 2. UVIT observation details.

Object	Proposal ID	NUV filter	NUV exposure time (s)	FUV filter	FUV exposure time (s)
(1)	(2)	(3)	(4)	(5)	(6)
MRK 306	A02_165	NUV – B13	1228	Sapphire	1446
MRK 721	A02_165	NUV – B13	1819	Sapphire	1841
MRK 789	A03_091	NUV – B13	2137	Sapphire	2137
MRK 739	A03_091	NUV – B13	2258	–	–
	A07_148	–	–	CaF2	6500
NGC 3773	A03_091	NUV – B13	2522	Sapphire	2484
ESO509–IG066	A03_091	NUV – B13	2207	Sapphire	1833
	A07_148	–	–	Sapphire	13470
SDSS J1436	A03_091	NUV – B13	2421	Sapphire	2426
SDSS J1019	A04_085	–	–	CaF2	4451
SDSS J1027	A04_085	Silica15	4986	CaF2	4958

Notes. Column 1: name of the objects. Column 2: UVIT proposal ID. MRK 739 and ESO509-IG066 have two observations. Columns 3 and 4: name of the NUV filters and exposure time of the observations. Columns 5 and 6: name of the FUV filters and exposure time of the observations.

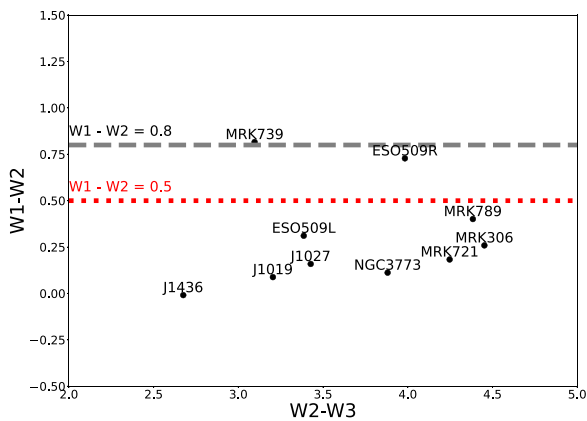


Figure 1. WISE colour–colour plot using $W1 - W2$ (mag) versus $W2 - W3$ (mag). The sample galaxies are plotted as black dots. Several colour cut-offs are present to separate the AGN emission from SF. We have used two such cut-offs: $W1 - W2 = 0.8$ for single AGN (Stern et al. 2012) while $W1 - W2 = 0.5$ for multiple AGN (Blecha et al. 2018). The dual AGN MRK 739 and the western nuclei of ESO509-IG066 fall above the limit.

305 is masked while making the colour map and radial profile (Fig. 2: lower panel), (ii) MRK 721: It is found that a QSO at redshift 0.745 (Fig. 3, upper right), coincides with one of the spiral arms of our sample galaxy MRK 721 (redshift 0.032, Table 1). We masked this with an aperture of radius 5 pixels as estimated from the SDSS image while performing photometry and making the colour map/profile (Fig. 3).

4.2 UV image analysis

4.2.1 Identification of clumps

To identify the SFCs, we have used the Source Extraction and Photometry (SEXTRACTOR; Bertin & Arnouts 1996) library from PYTHON. SEXTRACTOR can perform tasks like background subtraction, source detection and deblending on the fits format data files. The foreground and background sources were masked during this process. Initially, we set parameters like the threshold, which is the minimum count over which the source is defined, minimum area which is the minimum source area that has to be more than the PSF of the telescope to define a source and deblending count which

is used so that sources will not blend with each other. We set the threshold as 5σ , the minimum area as 10, and the deblending count as 0.0005. Therefore, the identification of SFCs involves a three-step process. Initially, all pixels exhibiting a signal-to-noise ratio (SNR) of 5σ or higher are chosen. Subsequently, a second criterion, which mandates a minimum contiguous area of 10 pixels, is applied. This 10-pixel threshold is implemented to prevent the detection of SFCs smaller than the UVIT PSF, ensuring confident detections. Finally, a deblending ratio based on contrast separates distinct clumps. These parameter choices result in reliable detections and are consistent with those used in related studies involving the identification of SFCs in UVIT images (Yadav et al. 2021a; Nandi et al. 2023). We have detected SFCs separately in FUV and NUV images and hence the clumps (as well as clump IDs) are different in FUV and NUV images (as shown in Figs 2–10). In a few cases, multiple clumps in one band get deblended as a single clump in another band. For example, in ESO509–IC066 (Fig. 7), two NUV SFCs (id 1 and 2) get deblended as one SFC (id 2) in the FUV image. The central region of ESO509–IC066 in the FUV image is exceptionally bright. This situation presents two possible scenarios, either the contrast within this region does not decrease below the given deblending count, or if the contrast does decrease, no more than 10 connected pixels surpass the specified threshold, thus making it challenging for SEXTRACTOR to identify separate clumps.

The images have been smoothed using a 2-pixel Gaussian Kernel, and contrast settings have been adjusted for improved visualization. Consequently, some regions may appear as clumps (e.g. SDSS J1436 FUV: Fig. 8), while others may seem relatively sparse (e.g. MRK 721). It is important to emphasize that the unsmoothed images were used to identify SFCs with SEXTRACTOR. In the appendix (Fig. A1), we provide the unsmoothed FUV image of SDSS J1436 to illustrate why SFCs are not detected there and an image of MRK 721, where the clumps appear relatively distinct with the given criteria, in our sample galaxies. SEXTRACTOR could detect 5–20 SFCs in some galaxies, but some of them have only 1–3 SFCs (Figs 2–10).

4.2.2 Aperture photometry

Aperture photometry is carried out to calculate the total counts of the galaxies as well as the counts in the detected SFCs. Here, we have used the PYTHON package *photutils* to perform aperture photometry. One of the important tasks for aperture photometry is the subtraction of the background. This is done by fitting apertures of the same size as

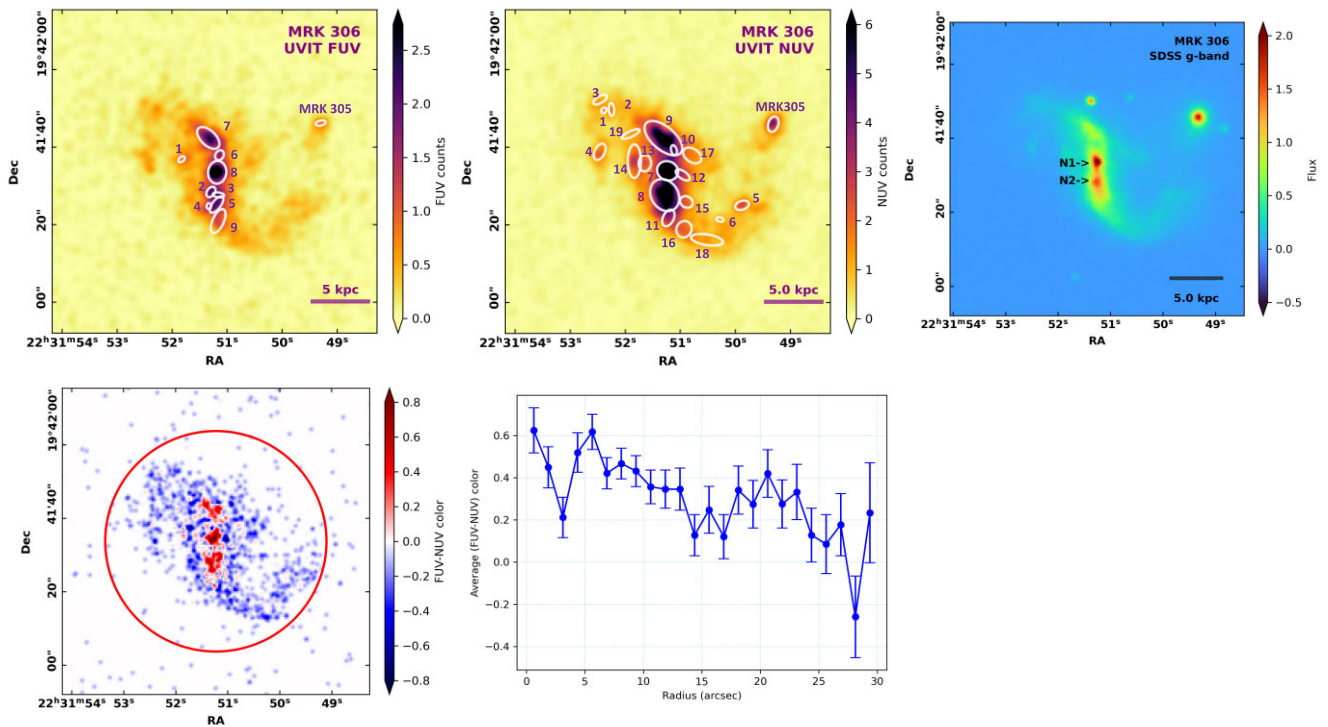


Figure 2. Multiband images of MRK 306 along with the detected SFCs. Upper left panel: the UVIT FUV image; upper middle: the UVIT NUV image; upper right panel: the SDSS *g*-band image indicating the dual nuclei; lower left panel: the FUV – NUV colour map; lower middle panel: the radial profile of FUV – NUV colour. This is obtained with the annulus (width = 3 pixels) starting from the centre till the red circle as shown on the colour map. The neighbour galaxy MRK 305 is masked while making the colour map and colour profile.

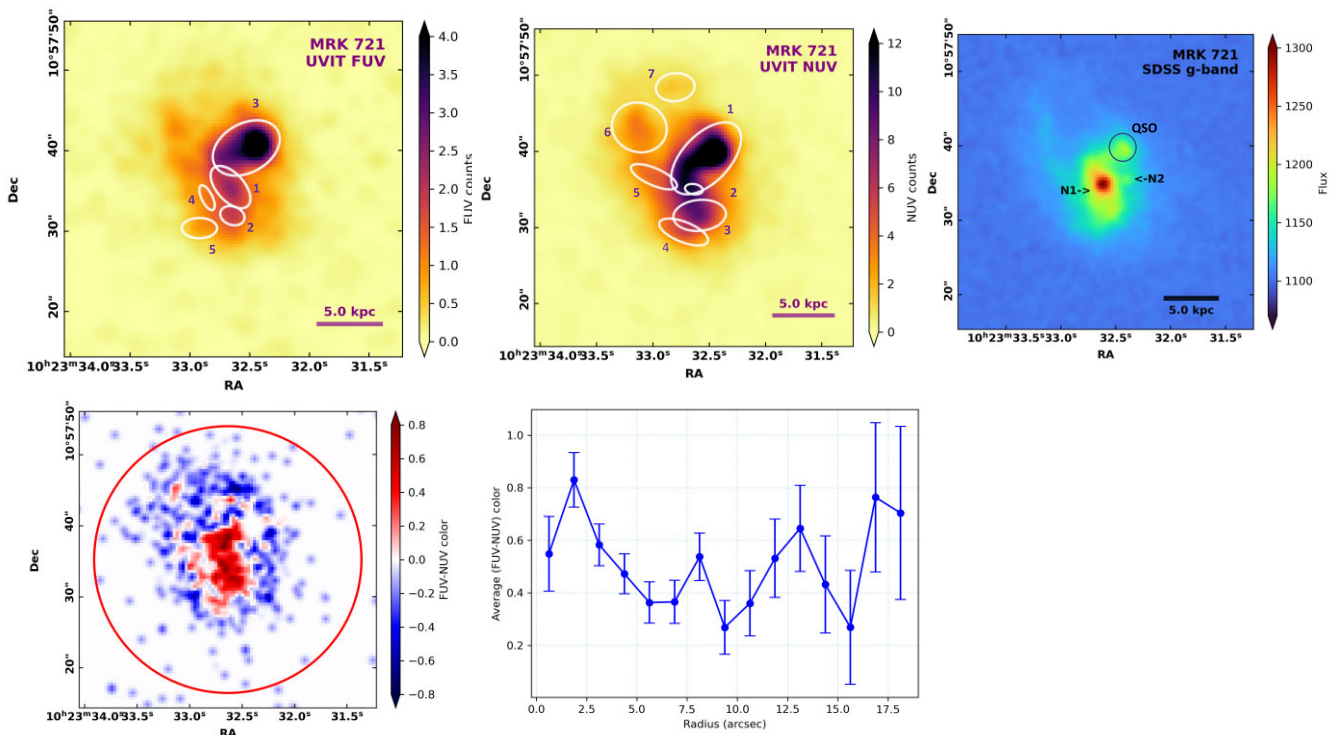


Figure 3. Multiband images of MRK 721. Same as Fig. 2. SFC no 3 in the FUV and SFC no 1 in the NUV images involve a bright source on the north-west which is assigned as a QSO source as shown in the SDSS image (upper right) with a black circle. While performing the photometry as well as the colour map, and colour profile, we masked the QSO with an aperture radius of 5 pixels.

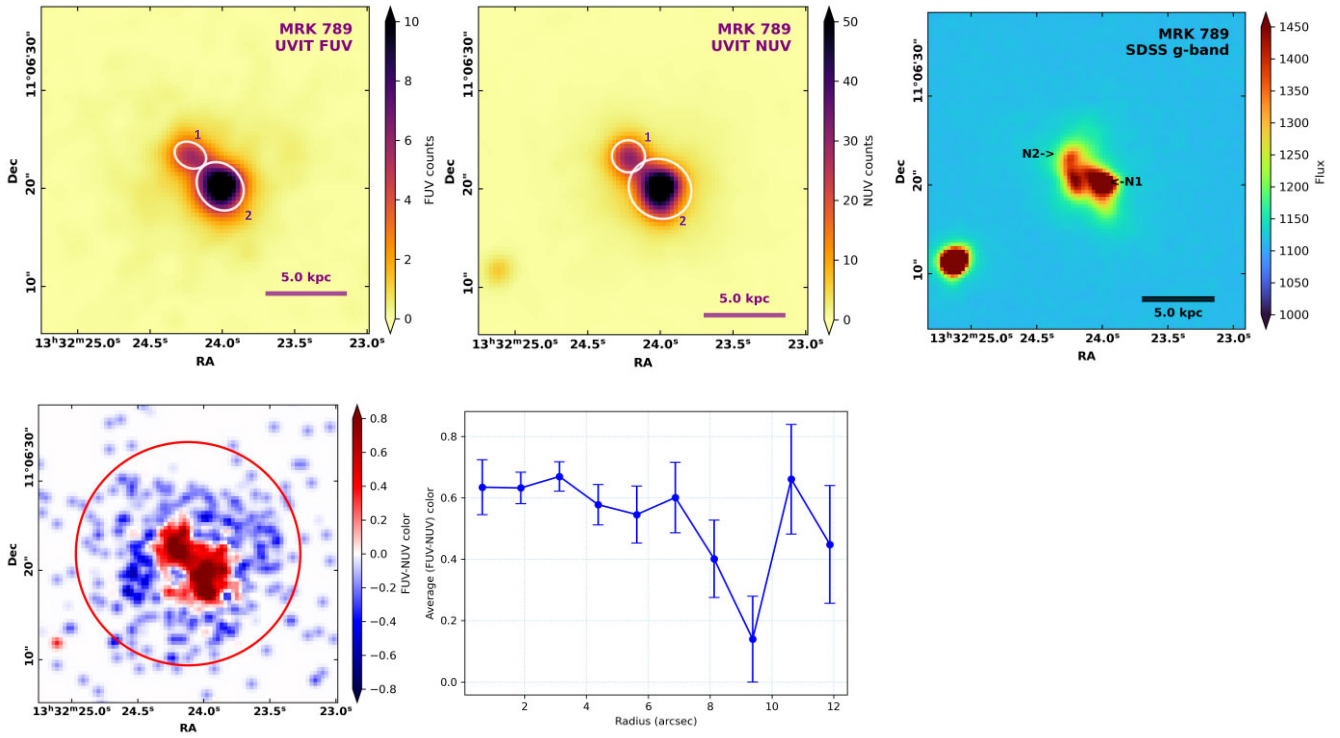


Figure 4. Multiband images of MRK 789. Same as Fig. 2.

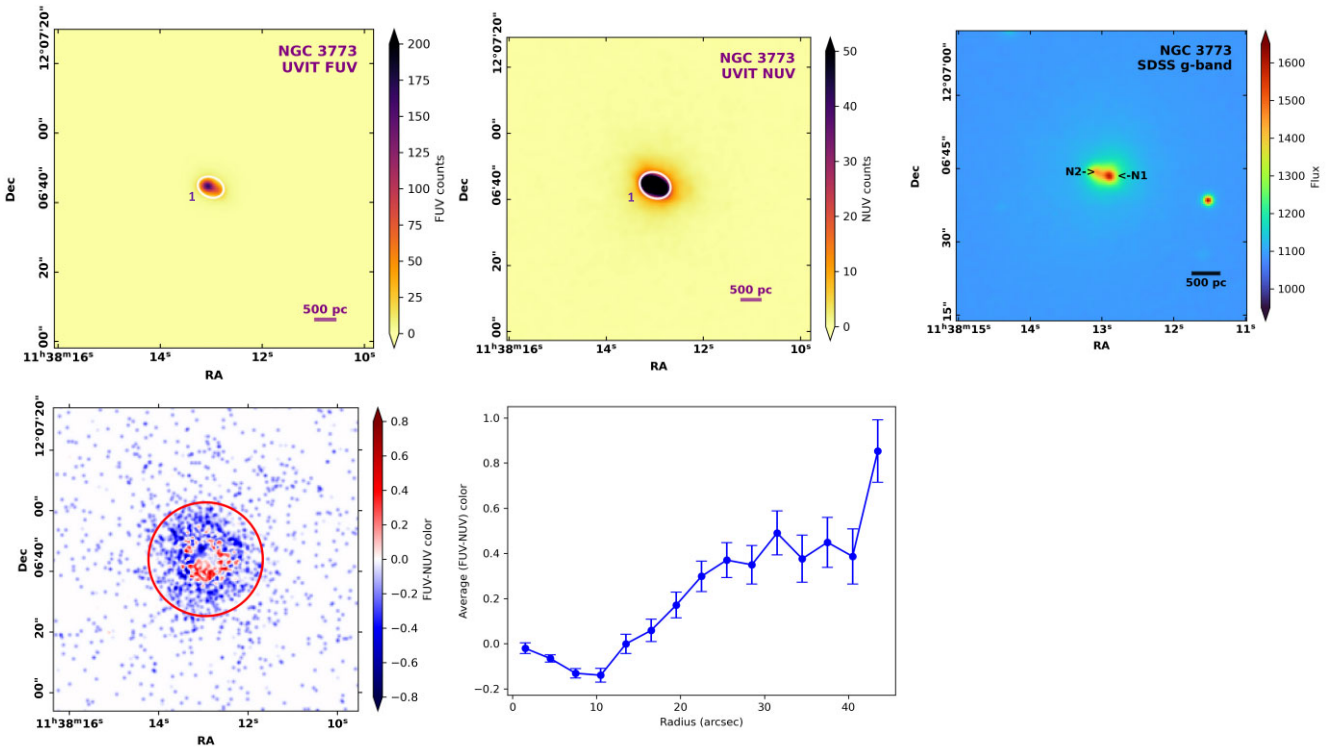


Figure 5. Multiband images of NGC 3773. Same as Fig. 2. The radial profile of FUV – NUV colour shows a blue colour in the nuclear region surrounded by redder emission which is opposite in the rest of the galaxies.

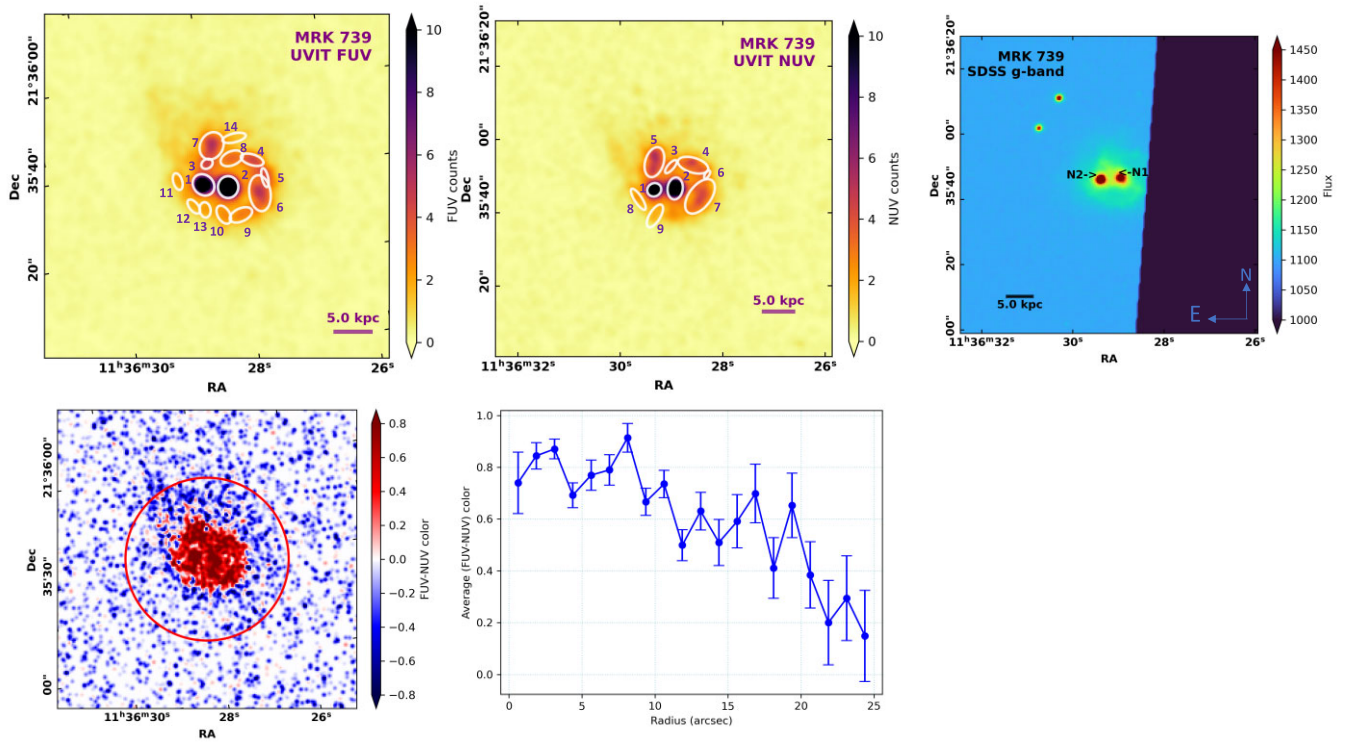


Figure 6. Multiband images of MRK 739. Same as Fig. 2. This hosts a dual pair of AGNs (SFC 1, 2). We have masked both the nuclear region with a 3-pixel aperture radius and then the photometry is done. The directions are shown with the arrows in the lower right corner of the optical SDSS image. SFC_{FUV} 3, 7 and SFC_{NUV} 5 are discussed further to explore AGN feedback effect in Section 5.4.

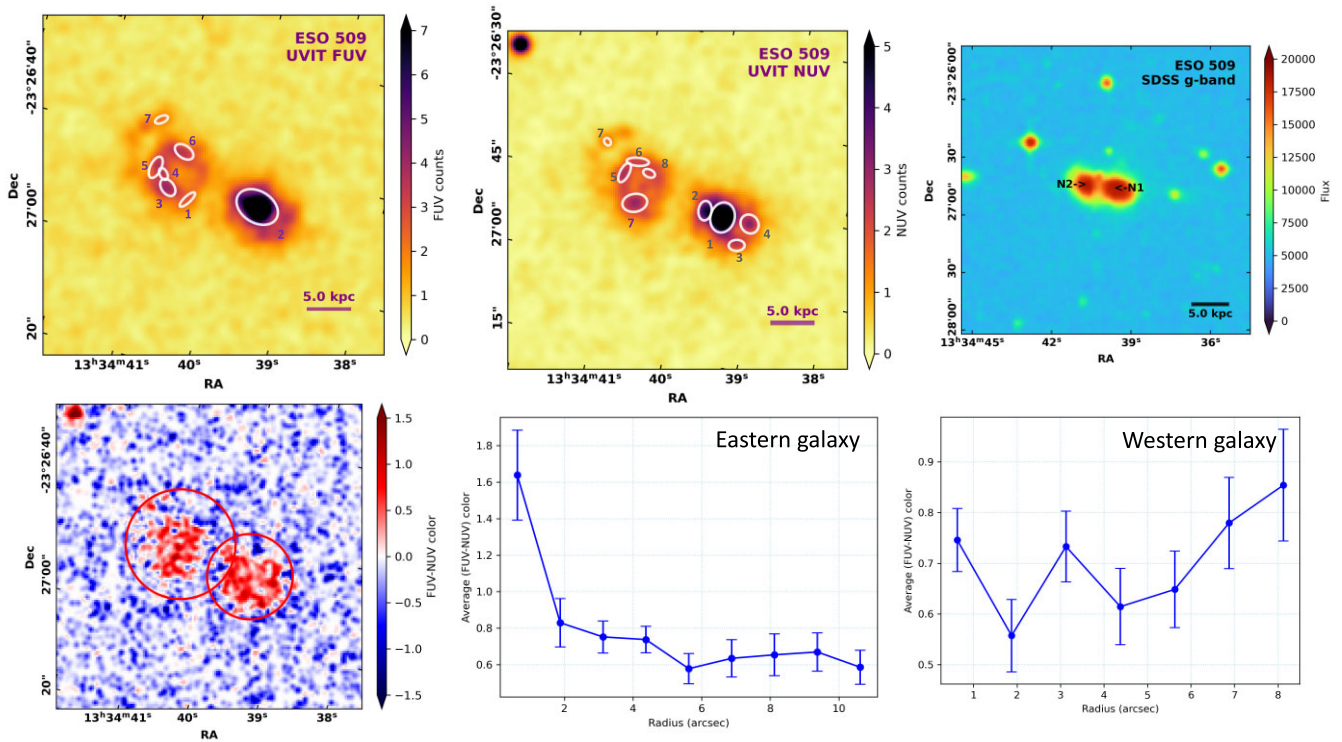


Figure 7. Multiband images of ESO509-IG066. Same as Fig. 2; as the parents’ galaxies are yet separated, those are treated as individuals in radial profile analyses and shown in the lower middle and lower right plots. The western nucleus was masked with an aperture of a 3-pixel radius while performing photometry. The eastern nucleus (left panel) is not detected in FUV image and is surrounded by SFC no 1, 3, 4, 5, and 6 in a ring shape (see Section 5.4). The direction of the images is same as Fig. 6.

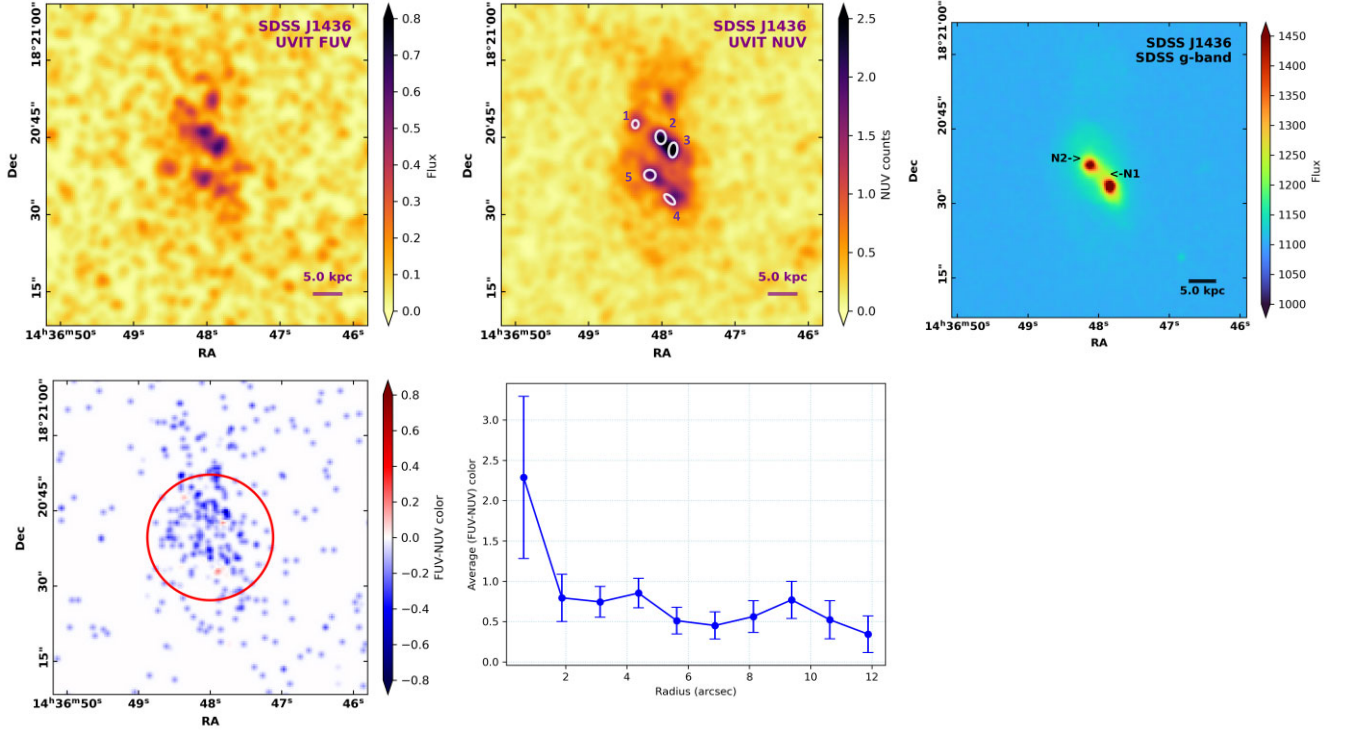


Figure 8. Multiband images of SDSS J1436. Same as Fig. 2. SEXTRACTOR could not detect any SFC in the FUV image.

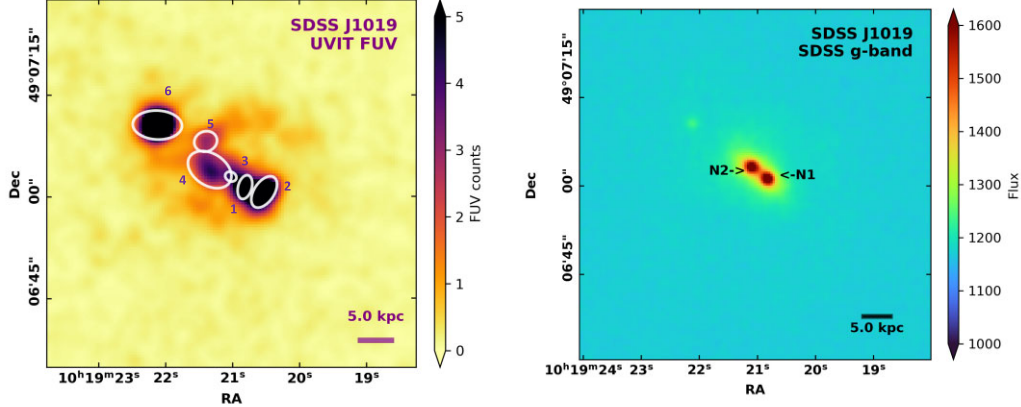


Figure 9. Multiband images of J1019. Left panel: the UVIT–FUV image. Right panel: the g-band optical image from SDSS. This system also hosts two AGNs. Though it is not an AGN-dominated system according to Fig. 1, as it shows the highest FUV SFR, we masked the AGN at the centres of SFC 1 and 3 with a 3-pixel aperture to minimize the AGN contribution (Tables 5 and 7).

the SFCs and the total galaxy in random source-free positions on the fits file. Then, we calculate the background and subtract those from the actual counts. To calculate the total counts from a galaxy, we have used the semimajor axis from the 2MASS K -band image or the R_{25} radius (Table 3). However, visual inspection was done before aperture photometry and whenever we find the UV emission more extended, we change the radius accordingly. These details are given in Table 3. This is to note that we have treated ESO 509–IG066 as a single system while performing the extinction calculation (Tables 3 and 4). However, as two galaxies (east and west) are still well separated, we have provided the total SFR of individual galaxies (Table 5). We have

used the position as well as the size along with the orientation of the SFCs from SEXTRACTOR to perform aperture photometry (Table 7).

4.2.3 Uncorrected magnitudes and extinction

The background-subtracted counts are converted into magnitude using the exposure time of the observations and the zero points, taken from (Tandon et al. 2020). The uncorrected magnitudes are given in Table 3. Next, we have corrected the Milky Way extinction using $E(B - V) \times R_V$, where $E(B - V)$ is the reddening and R_V is the extinction ratio. Here, $E(B - V)$ for our sample galaxies are obtained

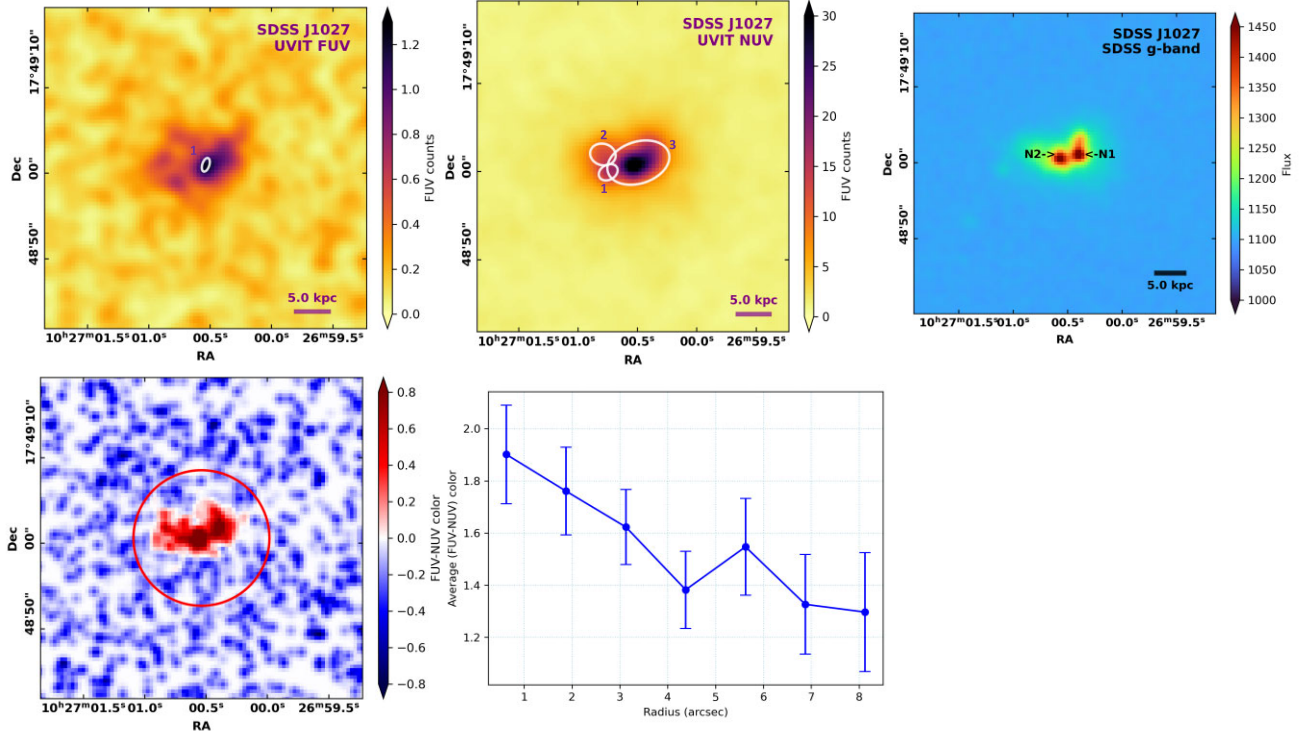


Figure 10. Multiband images of SDSS J1027. Same as Fig. 2.

Table 3. Magnitudes in FUV and NUV bands.

Name (1)	Radius (arcsec) (2)	Mag (UVIT)		Mag (<i>GALEX</i>)		Galactic $E(B - V)$ (7)	Corrected UVIT mag (Gal)		Total colour (FUV _{corr} - NUV _{corr}) (10)
		FUV (3)	NUV (4)	FUV (5)	NUV (6)		FUV _{corr} (8)	NUV _{corr} (9)	
MRK 306	47	16.45 ± 0.02	16.09 ± 0.01	16.51 ± 0.03	16.04 ± 0.02	0.0488	16.06 ± 0.02	15.70 ± 0.01	0.36 ± 0.02
MRK 721	21	17.48 ± 0.03	16.99 ± 0.01	17.37 ± 0.05	16.81 ± 0.03	0.0232	17.29 ± 0.03	16.80 ± 0.01	0.49 ± 0.02
MRK 789	26	17.38 ± 0.02	16.68 ± 0.01	17.40 ± 0.05	16.75 ± 0.02	0.0281	17.15 ± 0.02	16.46 ± 0.01	0.69 ± 0.02
NGC 3773	40	15.21 ± 0.01	15.23 ± 0.01	15.23 ± 0.01	14.97 ± 0.01	0.0233	15.03 ± 0.01	15.04 ± 0.01	-0.01 ± 0.01
MRK 739	25 ^a	17.77 ± 0.01	17.08 ± 0.01	17.46 ± 0.05	16.69 ± 0.02	0.0214	17.60 ± 0.01	16.91 ± 0.01	0.69 ± 0.01
ESO509-IG066	20 ^a	18.38 ± 0.01	17.84 ± 0.01	18.32 ± 0.10	17.73 ± 0.05	0.0951	17.61 ± 0.01	17.09 ± 0.01	0.52 ± 0.01
SDSS J1436	28	19.41 ± 0.05	18.59 ± 0.02	19.34 ± 0.13	18.57 ± 0.06	0.0247	19.21 ± 0.05	18.39 ± 0.02	0.82 ± 0.05
SDSS J1019	14 ^a	18.60 ± 0.02	-	18.59 ± 0.08	17.38 ± 0.03	0.0090	18.51 ± 0.08	17.31 ± 0.03	1.20 ± 0.08
SDSS J1027	19	21.19 ± 0.06	19.31 ± 0.01	21.07 ± 0.35	19.61 ± 0.13	0.0208	21.03 ± 0.06	19.15 ± 0.01	1.88 ± 0.06

^aVisual inspections are done before the analysis, and apertures are adjusted from eye estimation depending on the UV emission where required. *Notes.* Column (1): name of the objects. Column (2): the radius of the apertures to calculate the UVIT magnitudes. These are taken as half of the major axis defined by 2MASS or R_{25} . Column (3) and (4): the calculated magnitudes in the UVIT FUV and NUV bands. Columns (5) and (6): the *GALEX* FUV and NUV magnitudes. Column (7): the Galactic reddening. Columns (8) and (9): the Galactic extinction corrected UVIT magnitudes. As SDSS J1019 has only an FUV image from UVIT, we have corrected the *GALEX* magnitudes (FUV and NUV) and added them here. Column (10): the total colour of the galaxies, calculated using Columns (8) and (9).

from Schlafly & Finkbeiner (2011) which is available at IRSA page.⁶ We have taken R_{FUV} and R_{NUV} as 8.06 and 7.95, respectively (Bianchi 2011). In Table 3, we have provided the *GALEX* magnitudes (FUV and NUV) for comparison with the UVIT magnitudes as well as the Galactic extinction corrected UVIT magnitudes which are further used to calculate the colour of the galaxies.

Galaxies have internal dust that also absorbs UV light. This is why the calculated flux is always lower than the actual value. Several different approaches are adopted to correct for this absorption. We

have used UV spectral slope β ($f_{\lambda} \propto \lambda^{\beta}$) to calculate the colour excess. The following equation is used to calculate β from Nordon et al. (2013):

$$\beta = -\frac{m(\lambda_1) - m(\lambda_2)}{2.5 \log\left(\frac{\lambda_1}{\lambda_2}\right)} - 2. \quad (1)$$

Here, λ_1 and λ_2 are effective wavelength of the FUV and NUV filters, respectively, and $m(\lambda_1)$ and $m(\lambda_2)$ are the Milky way corrected magnitudes. More negative values of β imply the least dust while more positive values imply the more dusty system. The calculated β values are given in Table 4. The colour excess is calculated following

⁶<https://irsa.ipac.caltech.edu/applications/DUST/>

Table 4. Internal extinction calculation.

Name (1)	Total A_V calculation with radius from Column 2, Table 3										
	β (2)	Internal $E(B - V)$ (3)	A_{FUV} (mag) (4)	A_{NUV} (mag) (5)	Max (6)	A_{FUV} Min (7)	Mean (8)	Max (9)	A_{NUV} Min (10)	Mean (11)	
MRK 306	-1.21 ± 0.01	0.299 ± 0.003	1.30 ± 0.01	1.03 ± 0.01	1.85 ± 0.04	0.82 ± 0.21	1.29 ± 0.06	1.47 ± 0.03	0.65 ± 0.17	1.03 ± 0.05	
MRK 721	-0.92 ± 0.02	0.361 ± 0.003	1.50 ± 0.01	1.19 ± 0.01	2.27 ± 0.03	0.74 ± 0.19	1.55 ± 0.10	1.80 ± 0.02	0.59 ± 0.11	1.13 ± 0.09	
MRK 789	-0.48 ± 0.01	0.456 ± 0.002	1.99 ± 0.01	1.58 ± 0.01	1.94 ± 0.01	1.64 ± 0.04	1.82 ± 0.04	1.54 ± 0.01	1.34 ± 0.03	1.45 ± 0.03	
NGC 3773	-2.03 ± 0.13	0.123 ± 0.030	0.53 ± 0.13	0.44 ± 0.10	0.53 ± 0.23	0.28 ± 0.05	0.39 ± 0.05	0.42 ± 0.22	0.23 ± 0.04	0.31 ± 0.04	
MRK 739	-0.73 ± 0.01	0.402 ± 0.001	1.83 ± 0.01	1.40 ± 0.01	2.44 ± 0.01	1.59 ± 0.02	2.08 ± 0.07	1.94 ± 0.01	1.27 ± 0.02	1.66 ± 0.06	
ESO509-IG066	-0.84 ± 0.01	0.378 ± 0.002	1.65 ± 0.01	1.31 ± 0.01	2.57 ± 0.02	1.23 ± 0.14	1.95 ± 0.10	2.04 ± 0.02	0.98 ± 0.19	1.55 ± 0.08	
SDSS J1436	-0.20 ± 0.01	0.514 ± 0.004	2.23 ± 0.01	1.78 ± 0.01	2.32 ± 0.05	1.27 ± 0.16	1.83 ± 0.12	1.84 ± 0.04	1.01 ± 0.12	1.46 ± 0.10	
SDSS J1019 ^d	0.76 ± 0.02	0.723 ± 0.004	3.25 ± 0.02	2.62 ± 0.01	—	—	—	—	—	—	
SDSS J1027	1.53 ± 0.01	0.886 ± 0.002	4.04 ± 0.01	3.10 ± 0.01	4.08 ± 0.03	3.13 ± 0.03	3.16 ± 0.16	3.13 ± 0.21	2.40 ± 0.02	2.76 ± 0.16	

^aSDSS J1019 does not have UVIT NUV image, only total extinction values are given using GALEX FUV, NUV magnitudes. *Notes.* Columns: (1) Name of the objects. Column (2); the UV spectral slop (β). Column (3); the calculated reddening ($E(B - V)$). Columns (4) and (5); the total extinction for FUV and NUV bands. This is done with the radius quoted in Column 2 of Table 3. The fluxes are corrected for these extinction values before calculating the SFR (Table 5) and Σ_{SFR} (Table 7). Columns (6)–(11): The maximum, minimum, and mean values of extinction in the FUV and NUV bands are provided. These are average values and are obtained using the consecutive annulus with a radius of 3 pixels starting from the centre to the maximum radius till clumps are detected in the individual galaxy.

Reddy et al. (2018):

$$\beta = -2.616 + 4.684E(B - V). \quad (2)$$

Following (Calzetti et al. 2000), the extinction A_V is $E_s(B - V)K_\lambda$ where

$$K_\lambda = 2.659(-2.156 + 1.509/\lambda - 0.198/\lambda^2 + 0.011/\lambda^3) + R'_V \quad (3)$$

for $0.12 \leq \lambda \leq 0.63 \mu\text{m}$ and $E_s(B - V) = (0.44 \pm 0.03)E(B - V)$. The calculated values of A_{FUV} A_{NUV} are listed in Table 4.

The above task is done for the total galaxy (radius: Table 3) and these single values of A_{FUV} and A_{NUV} of individual galaxies (Table 4) are used to correct the SFR of the total galaxy as well as the SFR surface density of the SFC. Calculating the extinction of individual SFCs is difficult, especially when the SFCs are not distributed evenly on the disc. Here, we have tried to estimate the maximum, and minimum values of average A_V using annulus with increasing radius from centre to the maximum radius where outermost SFCs are detected. These values are listed in Table 4 for the reference. This is to note that the maximum and minimum A_V values can increase and decrease the SFR of SFCs up to 2.33 times and 0.39 times, respectively.

4.2.4 Colour maps and radial profiles

We have FUV and NUV maps for eight galaxies while one has only FUV data. To create colour maps, we first aligned the FUV and NUV images using *geomap* and *geotran* in IRAF. Then we used the background subtracted, integration-time-weighted images to create the NUV/FUV images. Next, we converted the NUV/FUV count ratio image to the magnitude scale using the zero point of the individual bands.

To understand the colour profile of the galaxies more quantitatively, we have calculated the average colour in consecutive annuli increasing outwards radially. We started from the galaxy centres and then used circular annuli from *photutils* and did aperture photometry for individual annuli in NUV and FUV bands. The annulus radius is kept at 3 pixels and extends up to the galactic emission (red circles in lower left images: Figs 2–10). Then, we converted the background subtracted counts to the magnitudes as above and calculated the colour by subtracting the FUV–NUV magnitude of the individual annuli. Finally, to examine the colour profile, we plotted the average colour with the aperture radius (lower middle: Figs 2–10).

4.3 Star formation rate and stellar mass estimation

The SFR and stellar mass provide crucial information about any galaxy. Hence, proper estimation of SFR is one of the most essential parts of understanding galaxies and their evolution. While the global SFR of a galaxy provides information about the global properties and is related to galaxy evolution, the local SFR within the galaxies helps us to understand the spatial variations, the SF trigger mechanisms as well as any feedback process. There are many calibrators to calculate SFR, but the UV photons emitted by the young stars are often taken as a good indicator of recent SFR. However, as mentioned above, the extinction correction is needed. We have derived UV extinction corrected SFR using the following formulas (Iglesias-Páramo et al. 2006; Cortese, Gavazzi & Boselli 2008) assuming a Salpeter initial mass function (IMF) from 0.1 to $100 M_\odot$ and solar metallicity:

$$\text{SFR}_{FUV}(M_\odot \text{yr}^{-1}) = \frac{L_{FUV}(\text{erg s}^{-1})}{3.83 \times 10^{33}} \times 10^{-9.51}, \quad (4)$$

Table 5. Total SFR.

Object (1)	Band (2)	Flux density ($\text{erg s}^{-1} \text{cm}^{-2} \text{\AA}^{-1}$) (3)	Luminosity (ergs s^{-1}) (4)	SFR ($M_{\odot} \text{yr}^{-1}$) (5)
MRK 306	FUV	$(5.28 \pm 0.09) \times 10^{-14}$	$(5.40 \pm 0.09) \times 10^{+43}$	4.36 ± 0.07
	NUV	$(2.46 \pm 0.02) \times 10^{-14}$	$(3.83 \pm 0.03) \times 10^{+43}$	3.09 ± 0.03
MRK 721	FUV	$(2.17 \pm 0.05) \times 10^{-14}$	$(8.20 \pm 0.20) \times 10^{+43}$	6.61 ± 0.15
	NUV	$(1.08 \pm 0.01) \times 10^{-14}$	$(6.24 \pm 0.08) \times 10^{+43}$	5.04 ± 0.06
MRK 789	FUV	$(3.63 \pm 0.07) \times 10^{-14}$	$(1.31 \pm 0.02) \times 10^{+44}$	10.58 ± 0.21
	NUV	$(1.94 \pm 0.01) \times 10^{-14}$	$(1.06 \pm 0.01) \times 10^{+44}$	8.60 ± 0.08
NGC 3773	FUV	$(6.74 \pm 0.04) \times 10^{-14}$	$(4.34 \pm 0.03) \times 10^{+42}$	0.350 ± 0.002
	NUV	$(2.56 \pm 0.01) \times 10^{-14}$	$(2.51 \pm 0.01) \times 10^{+42}$	0.203 ± 0.001
MRK 739	FUV	$(3.77 \pm 0.04) \times 10^{-14}$	$(1.22 \pm 0.01) \times 10^{+44}$	9.91 ± 0.10
	NUV	$(4.84 \pm 0.05) \times 10^{-14}$	$(1.45 \pm 0.02) \times 10^{+44}$	11.71 ± 0.13
ESO509–IG066 (east)	FUV	$(7.71 \pm 0.15) \times 10^{-15}$	$(3.07 \pm 0.06) \times 10^{+43}$	2.48 ± 0.04
	NUV	$(4.17 \pm 0.09) \times 10^{-15}$	$(2.53 \pm 0.05) \times 10^{+43}$	2.04 ± 0.04
ESO509–IG066 (west)	FUV	$(8.76 \pm 0.16) \times 10^{-15}$	$(3.49 \pm 0.06) \times 10^{+43}$	2.82 ± 0.05
	NUV	$(4.46 \pm 0.10) \times 10^{-15}$	$(2.70 \pm 0.06) \times 10^{+43}$	2.18 ± 0.05
SDSS J1436	FUV	$(6.89 \pm 0.34) \times 10^{-15}$	$(6.07 \pm 0.30) \times 10^{+43}$	4.90 ± 0.24
	NUV	$(4.11 \pm 0.08) \times 10^{-15}$	$(5.51 \pm 0.11) \times 10^{+43}$	4.45 ± 0.09
SDSS J1019	FUV	$(4.17 \pm 0.07) \times 10^{-14}$	$(4.08 \pm 0.07) \times 10^{+44}$	32.96 ± 0.62
SDSS J1027	FUV	$(8.59 \pm 0.05) \times 10^{-15}$	$(1.30 \pm 0.07) \times 10^{+44}$	10.55 ± 0.62
	NUV	$(6.83 \pm 0.07) \times 10^{-15}$	$(1.69 \pm 0.02) \times 10^{+44}$	13.70 ± 0.15

Notes. Column (1): name of the objects. Column (2): observation wavebands. Columns (3) and (4): extinction (external + internal) corrected flux density and luminosity. Column (5): total star formation rate.

Table 6. Stellar mass (M_{\star}) and sSFR.

Object (1)	$W1$ (mag) (2)	$W2$ (mag) (3)	M_{\star} (M_{\odot}) (4)	sSFR (yr^{-1}) (5)
MRK 306	12.27 ± 0.02	12.01 ± 0.02	$(2.24 \pm 0.41) \times 10^9$	$(2.07 \pm 0.48) \times 10^{-9}$
MRK 721	12.01 ± 0.02	11.82 ± 0.02	$(1.64 \pm 0.31) \times 10^{10}$	$(4.48 \pm 0.85) \times 10^{-10}$
MRK 789	11.07 ± 0.02	10.67 ± 0.02	$(1.04 \pm 0.18) \times 10^{10}$	$(1.02 \pm 0.18) \times 10^{-9}$
NGC 3773	11.47 ± 0.02	11.36 ± 0.02	$(6.98 \pm 1.27) \times 10^8$	$(5.01 \pm 0.92) \times 10^{-10}$
MRK 739	9.91 ± 0.02	9.09 ± 0.02	$(2.41 \pm 0.42) \times 10^9$	$(4.11 \pm 0.71) \times 10^{-9}$
ESO509–IG066 east	12.14 ± 0.02	11.83 ± 0.02	$(7.22 \pm 1.34) \times 10^9$	$(3.43 \pm 0.64) \times 10^{-10}$
ESO509–IG066 west	11.05 ± 0.02	10.32 ± 0.02	$(1.73 \pm 0.30) \times 10^9$	$(2.03 \pm 0.34) \times 10^{-9}$
SDSS J1436	11.41 ± 0.02	11.42 ± 0.02	$(2.05 \pm 0.37) \times 10^{11}$	$(2.39 \pm 0.45) \times 10^{-11}$
SDSS J1019	11.93 ± 0.02	11.84 ± 0.02	$(8.67 \pm 1.65) \times 10^{10}$	$(3.46 \pm 0.66) \times 10^{-10}$
SDSS J1027	12.05 ± 0.04	11.89 ± 0.04	$(7.94 \pm 2.40) \times 10^{10}$	$(1.33 \pm 0.40) \times 10^{-10}$

Notes. Column 1: name of the objects. Columns 2 and 3: *WISE* bands $W1$ and $W2$ magnitudes centred at 3.368 and 4.618 μm . Column 4: Stellar mass of the galaxies. Column 5: specific star formation rate calculated using total SFR from column 5 of Table 5 and stellar mass.

$$\text{SFR}_{\text{NUV}}(M_{\odot}\text{yr}^{-1}) = \frac{L_{\text{NUV}}(\text{erg s}^{-1})}{3.83 \times 10^{33}} \times 10^{-9.33}. \quad (5)$$

The extinction-corrected total SFR as well as the SFR surface density for individual SFCs are given in Tables 5 and 7, respectively. In the next section, while discussing the SFR, we also reference the SFR from available literature for comparison.

Although some of the sample galaxies have stellar masses available in the literature, they have been obtained using different survey data as well as different SED-fitting methods. So to avoid this inconsistency, we have calculated stellar masses using *WISE* $W1 - W2$ colour and $W1$ luminosity following Cluver et al. (2014):

$$\log_{10} M_{\text{Stellar}}/L_{w1} = -2.54(W_{3.4\mu\text{m}} - W_{4.6\mu\text{m}}) - 0.17 \quad (6)$$

with

$$L_{w1}(L_{\odot}) = 10^{-0.4(M - M_{\text{SUN}})}, \quad (7)$$

where M is the absolute $W1$ magnitude of the source in $W1$ and $M_{\text{SUN}} = 3.24$. The stellar masses are listed in Table 6. We have calculated the sSFR ($\text{sSFR} = \text{SFR}/M_{\star}$) of our galaxies (Table 6) using the total extinction corrected FUV SFR (Table 5) and stellar mass.

5 RESULTS AND DISCUSSION

5.1 Extinction corrected global SFR and sSFR

SF in galaxies produces UV photons in bulk but a significant fraction of the light is absorbed by interstellar dust. Buat et al. (2009)

Table 7. Surface density of SFR (Σ_{SFR}) of the SFCs.

SFC no.	RA (J2000) (hh:mm:ss)	Dec. (J2000) (dd:mm:ss)	Semimajor (arcsec)	Seminor (arcsec)	Area (kpc ²)	PA (radian)	Σ_{SFR} ($M_{\odot} \text{ yr}^{-1} \text{ kpc}^{-2}$)
(1)	(2)	(3)	(4)	(5)	(6)	(7)	(8)
MRK 306 FUV							
1	22:31:51.83	19:41:36.83	0.97	0.58	0.20	-0.67	0.0842 ± 0.0229
2	22:31:51.29	19:41:28.40	1.46	0.98	0.52	-0.94	0.1442 ± 0.0185
3	22:31:51.15	19:41:27.65	1.46	0.60	0.32	0.11	0.1471 ± 0.0237
4	22:31:51.33	19:41:24.76	0.75	0.57	0.16	-1.40	0.1544 ± 0.0349
5	22:31:51.19	19:41:25.15	2.48	1.07	0.96	-0.92	0.1288 ± 0.0128
6	22:31:51.14	19:41:37.88	1.33	1.04	0.50	-1.04	0.1176 ± 0.0170
7	22:31:51.34	19:41:42.34	3.46	1.89	2.37	0.77	0.1156 ± 0.0077
8	22:31:51.18	19:41:33.48	2.90	2.32	2.44	-1.47	0.1596 ± 0.0090
9	22:31:51.16	19:41:20.88	3.29	1.42	1.70	-1.15	0.0584 ± 0.0065
MRK 306 NUV							
1	22:31:52.39	19:41:49.45	0.78	0.63	0.18	-1.00	0.0423 ± 0.0100
2	22:31:52.25	19:41:49.70	1.62	0.68	0.4	1.50	0.0384 ± 0.0064
3	22:31:52.45	19:41:52.24	1.92	0.88	0.61	-0.54	0.0249 ± 0.0041
4	22:31:52.46	19:41:38.80	2.24	1.27	1.03	-1.11	0.0431 ± 0.0042
5	22:31:49.88	19:41:25.01	1.78	1.12	0.72	-0.32	0.0609 ± 0.0060
6	22:31:50.28	19:41:21.34	0.96	0.54	0.19	0.20	0.0437 ± 0.0099
7	22:31:51.23	19:41:33.91	2.70	2.40	2.35	0.43	0.1957 ± 0.0059
8	22:31:51.28	19:41:27.64	4.30	3.41	5.33	1.00	0.1169 ± 0.0030
9	22:31:51.30	19:41:42.32	5.76	2.92	6.11	0.71	0.0963 ± 0.0026
10	22:31:51.11	19:41:39.20	1.30	0.71	0.34	1.33	0.1276 ± 0.0127
11	22:31:51.21	19:41:21.75	2.24	1.36	1.11	-1.11	0.0684 ± 0.0051
12	22:31:50.95	19:41:32.83	2.06	0.96	0.72	0.60	0.0652 ± 0.0062
13	22:31:51.64	19:41:35.87	2.08	1.57	1.19	-1.52	0.0447 ± 0.0040
14	22:31:51.83	19:41:36.40	4.26	1.66	2.57	-1.57	0.0456 ± 0.0027
15	22:31:50.89	19:41:25.88	1.68	1.38	0.84	0.58	0.0400 ± 0.0045
16	22:31:50.93	19:41:18.85	2.14	1.90	1.48	-1.15	0.0446 ± 0.0036
17	22:31:50.78	19:41:37.85	2.55	1.68	1.56	0.60	0.0337 ± 0.0030
18	22:31:50.51	19:41:16.13	4.06	1.35	1.99	0.16	0.0250 ± 0.0023
19	22:31:51.90	19:41:43.37	2.45	0.73	0.65	-0.44	0.0269 ± 0.0042
MRK 721 FUV							
1	10:23:32.66	10:57:35.44	3.11	1.67	6.48	0.85	0.1072 ± 0.0078
2	10:23:32.64	10:57:31.89	1.52	1.13	2.14	0.36	0.1154 ± 0.0141
3	10:23:32.53	10:57:40.31	4.37	2.98	16.24	-0.52	0.0915 ± 0.0046
4	10:23:32.86	10:57:34.13	1.66	0.66	1.37	1.12	0.0759 ± 0.0144
5	10:23:32.92	10:57:30.35	2.15	1.24	3.32	0.0	0.0452 ± 0.0071
MRK 721 NUV							
1	10:23:32.53	10:57:39.06	5.70	3.07	21.82	-0.82	0.0985 ± 0.0022
2	10:23:32.63	10:57:35.01	1.16	0.67	0.97	0.16	0.1898 ± 0.0143
3	10:23:32.58	10:57:31.57	3.39	2.0	8.45	-0.09	0.1058 ± 0.0036
4	10:23:32.73	10:57:29.39	3.35	1.30	5.43	0.38	0.0070 ± 0.0037
5	10:23:32.99	10:57:36.64	3.21	1.1	4.40	0.41	0.0662 ± 0.0040
6	10:23:33.12	10:57:43.12	3.57	3.17	14.11	0.34	0.0358 ± 0.0016
7	10:23:32.80	10:57:48.40	2.50	1.81	5.64	-0.12	0.0196 ± 0.0019
MRK 789 FUV							
1	13:32:24.22	11:06:23.37	1.66	1.25	2.52	0.50	0.3974 ± 0.0268
2 ^a	13:32:24.01	11:06:20.19	2.61	2.16	6.83	0.88	≤0.6596 ± 0.0210
MRK 789 NUV							
1	13:32:24.22	11:06:23.31	1.66	1.60	3.21	0.27	0.4973 ± 0.0136
2	13:32:24.00 ^a	11:06:20.00	3.20	2.92	11.28	0.56	≤0.6025 ± 0.0080
NGC 3773 FUV							
1	11:38:13.00	12:06:44.37	3.78	2.86	0.26	0.38	0.9069 ± 0.0079
NGC 3773 NUV							
1	11:38:12.99	12:06:44.19	4.73	3.82	0.44	0.4	0.4869 ± 0.0026
MRK 739 FUV							
1	11:36:28.22	21:35:31.15	2.64	2.23	6.44	0.76	0.0589 ± 0.0026
2	11:36:27.82	21:35:30.65	2.48	2.30	6.24	-1.56	0.1055 ± 0.0035
3	11:36:28.16	21:35:35.94	1.36	1.05	1.56	-0.54	0.0569 ± 0.0052
4	11:36:27.42	21:35:36.86	2.67	1.22	3.55	0.30	0.0504 ± 0.0032
5	11:36:27.22	21:35:32.79	2.17	0.71	1.68	1.34	0.0517 ± 0.0047

Table 7 – *continued*

SFC no.	RA (J2000) (hh:mm:ss)	Dec. (J2000) (dd:mm:ss)	Semimajor (arcsec)	Semiminor (arcsec)	Area (kpc ²)	PA (radian)	Σ_{SFR} (M _⊙ yr ⁻¹ kpc ⁻²)
(1)	(2)	(3)	(4)	(5)	(6)	(7)	(8)
6	11:36:27.30	21:35:29.25	4.10	2.41	10.8	1.43	0.0444 ± 0.0017
7	11:36:28.08	21:35:40.03	3.21	2.60	9.11	-1.10	0.0457 ± 0.0019
8	11:36:27.76	21:35:37.20	2.66	1.57	4.58	-0.41	0.0356 ± 0.0024
9	11:36:27.61	21:35:24.32	2.71	1.47	4.35	-0.42	0.0319 ± 0.0023
10	11:36:27.89	21:35:24.37	2.25	1.36	3.35	1.03	0.0279 ± 0.0025
11	11:36:28.64	21:35:31.90	1.95	1.01	2.16	1.27	0.0281 ± 0.0031
12	11:36:28.37	21:35:26.22	1.90	0.98	2.03	0.89	0.0217 ± 0.0028
13	11:36:28.19	21:35:25.46	1.75	1.25	2.39	1.41	0.0247 ± 0.0028
14	11:36:27.72	21:35:41.84	2.70	1.00	2.97	-0.23	0.0204 ± 0.0022
MRK 739 NUV							
1	11:36:29.34	21:35:46.22	1.93	1.74	3.67	-0.55	0.1877 ± 0.0105
2	11:36:28.93	21:35:46.59	2.98	2.03	6.62	-1.44	0.2538 ± 0.0091
3	11:36:29.01	21:35:52.55	2.22	0.82	1.99	-0.86	0.1191 ± 0.0114
4	11:36:28.58	21:35:52.94	4.20	1.99	9.14	0.29	0.1227 ± 0.0054
5	11:36:29.33	21:35:53.78	4.15	2.46	11.16	-1.27	0.1447 ± 0.0053
6	11:36:28.30	21:35:50.40	1.23	0.56	0.75	-0.99	0.1608 ± 0.0215
7	11:36:28.44	21:35:44.41	5.36	2.94	17.23	-0.92	0.1021 ± 0.0036
8	11:36:29.65	21:35:43.64	3.32	1.01	3.67	1.00	0.0768 ± 0.0067
9	11:36:29.32	21:35:39.09	3.46	1.45	5.49	-1.02	0.0468 ± 0.0043
ESO509-IG066 FUV							
1	13:34:42.80	-23:26:49.28	1.81	0.59	1.42	-0.75	0.0072 ± 0.0006
2	13:34:41.90	-23:26:50.60	4.04	2.85	15.28	0.57	0.0116 ± 0.0002
3	13:34:43.05	-23:26:47.13	1.74	1.14	2.64	0.94	0.0089 ± 0.0005
4	13:34:43.11	-23:26:44.73	1.16	0.68	1.05	1.10	0.0082 ± 0.0007
5	13:34:43.21	-23:26:43.56	2.08	0.98	2.71	-1.12	0.0064 ± 0.0004
6	13:34:42.84	-23:26:40.81	1.87	1.14	2.82	0.60	0.0071 ± 0.0004
7	13:34:43.13	-23:26:35.07	1.25	0.62	1.02	-0.40	0.0066 ± 0.0007
ESO509-IG066 NUV							
1	13:34:42.30	-23:26:53.88	2.77	2.20	8.08	-1.31	0.0414 ± 0.0022
2	13:34:42.53	-23:26:52.64	1.78	1.20	2.83	-1.43	0.0549 ± 0.0042
3	13:34:42.12	-23:26:58.91	1.45	1.00	1.93	-0.02	0.0303 ± 0.0038
4	13:34:41.95	-23:26:55.05	1.79	1.59	3.76	0.99	0.0318 ± 0.0028
5	13:34:43.58	-23:26:45.78	1.92	0.83	2.11	-1.09	0.0400 ± 0.0042
6	13:34:43.41	-23:26:43.82	2.01	0.74	1.99	0.08	0.0358 ± 0.0041
7	13:34:43.45	-23:26:51.23	2.27	1.63	4.91	-0.18	0.0312 ± 0.0024
8	13:34:43.26	-23:26:45.91	1.12	0.71	1.06	0.41	0.0308 ± 0.0052
9	13:34:43.81	-23:26:40.21	0.73	0.56	0.54	0.95	0.0334 ± 0.0075
SDSS J1436 NUV							
1	14:36:48.36	18:20:47.55	0.76	0.61	1.29	-1.5	0.0428 ± 0.0100
2	14:36:47.85	18:20:42.53	1.42	0.82	3.23	-1.44	0.0681 ± 0.0080
3	14:36:48.01	18:20:45.00	1.30	0.98	3.54	1.45	0.0504 ± 0.0066
4	14:36:47.89	18:20:32.94	1.28	0.59	2.10	0.75	0.0387 ± 0.0075
5	14:36:48.16	18:20:37.66	1.09	1.00	3.03	0.19	0.0484 ± 0.0070
SDSS J1019 FUV ^b							
1	10:19:20.82	49:07:01.42	1.77	0.99	5.73	-1.31	0.0640 ± 0.0115
2	10:19:20.53	49:07:00.70	2.56	1.45	12.13	-0.98	0.5434 ± 0.0230
3	10:19:21.03	49:07:02.96	0.84	0.68	1.87	0.48	NAN
4	10:19:21.34	49:07:04.00	3.43	2.31	25.9	0.58	0.1806 ± 0.0091
5	10:19:21.40	49:07:08.16	1.67	1.46	7.97	-0.37	0.1790 ± 0.0163
SDSS J1027 FUV							
1 ^a	10:27:00.53	17:49:00.97	0.81	0.40	1.59	-1.25	≤0.2663 ± 0.079
SDSS J1027 NUV							
1	10:27:00.75	17:48:59.91	1.17	0.85	4.82	-0.44	0.2148 ± 0.0111
2	10:27:00.49	17:49:01.00	3.76	2.34	42.89	-0.28	0.1852 ± 0.0034
3 ^a	10:27:00.79	17:49:01.92	1.53	1.20	8.96	0.22	≤0.1193 ± 0.006

^aSFCs have AGN included which may have contributed to the UV emission (though not dominated according to Fig. 1). Hence, the true values can be equal or less than the quoted values. ^bSFCs 1 and 3 of SDSS J1019 are masked (radius: 3 pixels) to minimize the AGN where SFC 3 gets fully masked and provides NAN value *Notes*. Column (1): The number of SFCs detected in the FUV and NUV images. Columns (2) and (3): RA and Dec. of the central position of SFCs. Columns (4) and (5): semimajor and semiminor axis in arcsec. Column (6): area of the SFCs. Column (7): position angle in radian. Column (8): the SFR density.

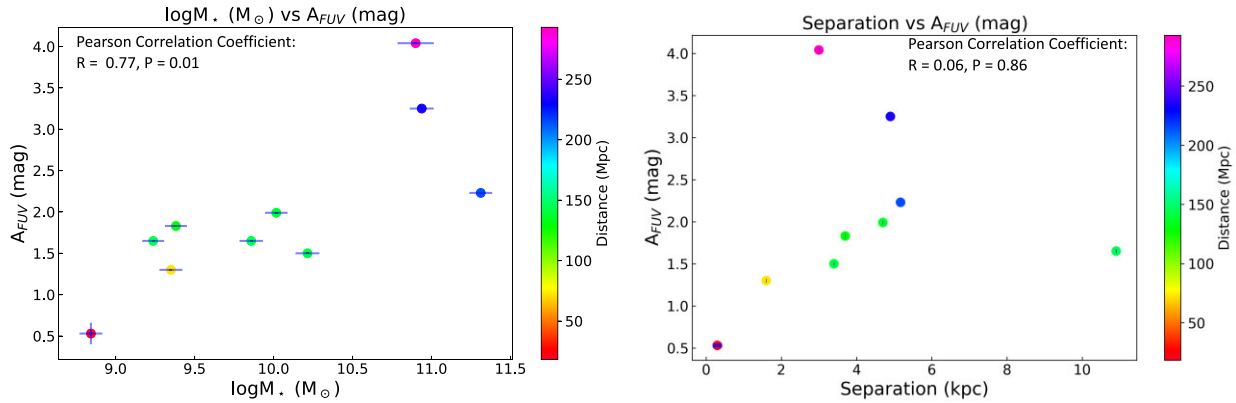


Figure 11. The correlation between the extinction and stellar mass (left panel), separation of the nuclei (right panel). While it shows a good correlation with the stellar mass, there is no correlation with the nuclear separations. The correlation coefficients are given in the upper corners.

suggested that the internal extinction in galaxies can be sometimes quite large and should be taken care of while using UV emission to estimate SFRs. We have attempted to calculate the dust attenuation in our sample galaxies using the UV continuum slope (β) which is assumed to be the deviation from the inherent recent SF (Meurer et al. 1995; Buat et al. 2009; Hao et al. 2011; Pannella et al. 2015). In a recent study with the UVIT, Pandey, Saha & Pradhan (2021) have found β to range from -2.72 to -0.60 for six star-forming galaxies in the Bootes Void ($z \sim 0.043-0.57$).

Goldader et al. (2002) studied bright IR galaxies and calculated β values at different aperture radii. While the β range from -1.42 to 4.41 in the central 0.5 Kpc, the average values over the total galaxy are $\beta = -1.35$ to -0.09 . This shows that dust attenuation varies from the centre of galaxies to the outskirts. Similarly, Yuan et al. (2012) studied a sample of galaxy pairs to understand the dust properties during mergers and compared it with a control sample of isolated galaxies. They found that while the β value ranges from ~ -1.5 to ~ 1 in isolated galaxies, the galaxy pairs have more scatter in β , with values ranging from ~ -3 to ~ 3 .

The calculated β of our sample galaxies falls in the range of the above-mentioned studies. Our calculated β parameters range from -2.03 ± 0.13 to 1.53 ± 0.01 (Table 4). The more negative β implies less dust obscuration while values close to zero or positive values imply more dust obscuration. As dual nuclei are the expected outcome of galaxy mergers, dust is expected in these galaxies. The calculated A_{FUV} and A_{NUV} ranges from 0.53 ± 0.13 to 4.04 ± 0.13 and 0.44 ± 0.10 to 3.10 ± 0.01 for our sample (Table 4). These values are calculated for the total galaxy with the aperture given in Table 3.

We have also explored the correlation between A_{FUV} versus stellar mass (M_*) and the separation of the nuclei (Fig. 11). This is because a smaller separation of galaxy pairs may indicate a later stage in galaxy mergers. Hence, both the dust mass, as well as dust distribution, can be different in the later stages of galaxy mergers compared to the early stages. We find that stellar mass and A_{FUV} are correlated with a correlation coefficient value of $R = 0.77$, $P = 0.01$. However, there is no significant correlation between A_{FUV} and separation with $R = 0.06$ and $P = 0.86$. Yuan et al. (2012) found a range of $A_{FUV} = 0.66$ to 5.26 for their galaxy pair sample. They have also checked the dependencies of A_{FUV} on the separation of the pairs along with the stellar mass. Their data show that A_{FUV} increases with stellar mass but it did not show any dependency on separation.

We have corrected the observed FUV and NUV fluxes for the Milky Way extinction as well as galaxy internal extinction for the sample. As some of our sample galaxies have very high extinction values, the SFRs increase by a factor of ~ 2 to ~ 48 times. One such example is the study of post-merger galaxy NGC 7252 by George et al. (2018c). They have found that the SFR derived from FUV emission from the main disc is $0.66 \pm 0.01 M_\odot \text{ yr}^{-1}$ whereas other indicators show much higher values (SFR IR/1.4 GHz/H α : $8.1/(6.3 \pm 0.2)/(5.6 \pm 1.1) M_\odot \text{ yr}^{-1}$ Schweizer et al. 2013). Furthermore, their estimation of A_{FUV} turned out to be 2.33 mag which can attenuate the actual UV light by eight times.

The extinction-corrected SFR for both the bands are given in Table 5. SDSS J1019 (Fig. 9) showed the highest FUV SFR. Here, we have re-estimated the SFR after masking the nuclei. The final SFR ranges from $\sim 0.35 \pm 0.01$ to $32.96 \pm 0.62 M_\odot \text{ yr}^{-1}$. The NUV SFR ranges from 0.203 ± 0.001 to $13.70 \pm 0.15 M_\odot \text{ yr}^{-1}$. The high SFR may be an outcome of the SF associated with the galaxy mergers. This is just to mention that the sample galaxies are also UV-rich according to our selection criteria (Section 2). Further, we have tried to compare the SFR with the available literature. However, it should be noted that there are several methods to estimate the SFR which can produce quite different values depending on the inputs.

We have found an extinction corrected $\text{SFR}_{FUV} = 9.91 \pm 0.10 M_\odot \text{ yr}^{-1}$ for MRK 739 where the emission from both nuclei (~ 1.2 arcsec) are masked. The uncorrected SFR is $1.55 \pm 0.01 M_\odot \text{ yr}^{-1}$. The SFR_{FIR} is reported as $6.9 M_\odot \text{ yr}^{-1}$ in Tubín et al. (2021). The triple AGN candidate SDSS J1027 in our sample has an $\text{SFR}_{FUV} = 10.55 \pm 0.62 M_\odot \text{ yr}^{-1}$ whereas Foord et al. (2021) reported SFR_{IR} as $18.2 \pm 1.3 M_\odot \text{ yr}^{-1}$. MRK 789 is a starburst merger galaxy, and we have found the $\text{SFR}_{FUV} = 10.58 \pm 0.21 M_\odot \text{ yr}^{-1}$, whereas the SED-produced SFR is $5.99 \pm 1.12 M_\odot \text{ yr}^{-1}$ (Salim et al. 2016). The overall analysis shows that the dual nuclei sample galaxies are dusty systems with high SFRs which may be the outcome of mergers.

Galaxy SFRs are found to increase with decreasing galaxy separation in some of the large statistical samples (Ellison et al. 2008). However, it depends on several factors such as galaxy masses, their mass ratios, prograde/retrograde orbits, and gas content. We checked whether the SFRs have any correlation with the separation of the nuclei. It shows that there is no correlation as the Pearson correlation coefficient is $R = -0.07$ and $P = 0.83$ for SFR_{FUV} ; also $R = -0.21$ and $P = 0.56$ for SFR_{NUV} (Fig. 12). However, it should be noted that our sample number is very small and inhomogeneous in terms

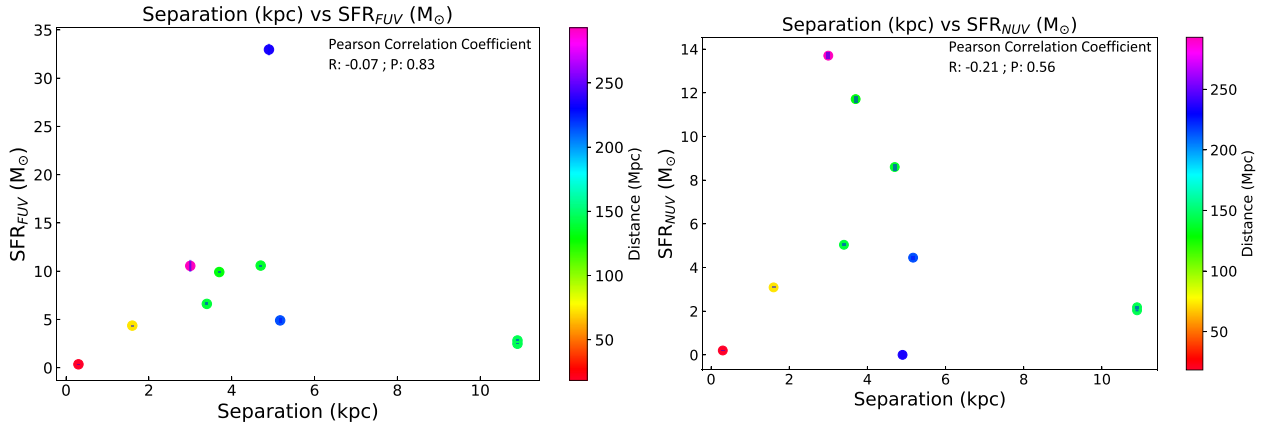


Figure 12. The correlation between the SFR_{FUV} (left panel), SFR_{NUV} (right panel) with the nuclear separation. It shows no correlation.

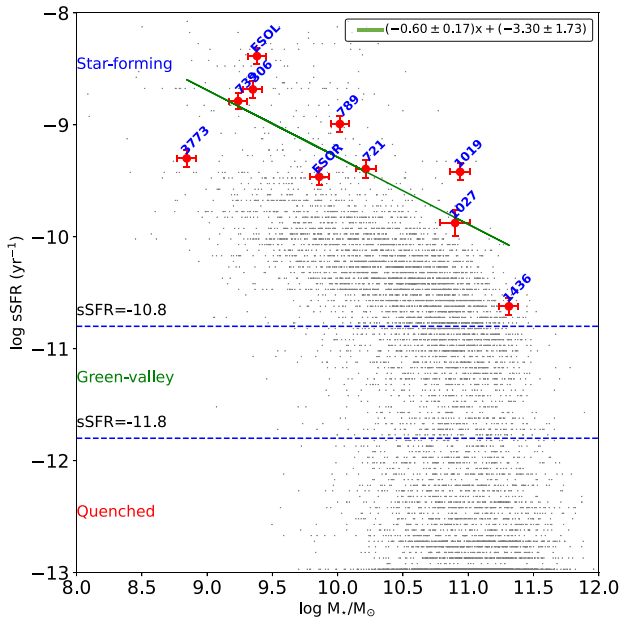


Figure 13. The logarithmic plot of specific SFR (sSFR) versus stellar mass (M_*) (Table 6). Our sample galaxies are in red dots. The star-forming region and green valley are divided at $\text{sSFR} = -10.8$ while the quenched region of the plot is divided at $\text{sSFR} = -11.8$. All of our sample galaxies are in the star-forming regions. The grey points in the background are galaxy data taken from Bait, Barway & Wadadekar (2017).

of redshift or separation. Hence, this result is limited and hard to compare with the results from larger unbiased samples.

The range of the calculated stellar masses is $(6.98 \pm 1.27) \times 10^8$ to $(2.05 \pm 0.37) \times 10^{11} M_\odot$ (Table 6). The stellar mass (M_*) and specific SFR (sSFR) are correlated for the star-forming galaxies and this is known as the star-forming main sequence. The $\text{sSFR}-M_*$ is one of the most important parameters to estimate the current level of SF in a galaxy for the available stellar material. It also indicates whether a galaxy is going through extensive SF or is in a quenched phase. Our calculated $\log(\text{sSFR})$ ranges from -10.26 ± 0.07 to $-8.38 \pm 0.07 \text{ yr}^{-1}$. All of the sample galaxies fall in the star-forming region (Fig. 13) which means that they are still actively forming stars. This is one of the expected results of our study of SF in dual nuclei galaxies. We have plotted M_* -sSFR (Fig. 13) with a control

sample from Bait, Barway & Wadadekar (2017) which studied 6000 galaxies in the local Universe to understand the dependence of SF on the morphological types.

We have fitted the data points in Fig. 13 and found a trend of sSFR decreasing with increasing stellar mass. Next, we checked the Pearson Correlation Coefficient which turned out to be $R = -0.775$, $P = 0.008$ signifying an anticorrelation. We fitted the data points with $\log(\text{sSFR}) \text{ yr}^{-1} = (-0.60 \pm 0.17) \log M_* M_\odot + (-3.30 \pm 1.73)$. Yuan et al. (2012) have found a similar trend where $x, y = -0.30, -7.28$ for their spiral pairs and $x, y = -0.53, -4.94$ for the control sample.

Tubín et al. (2021) studied dual AGN MRK 739 with high-resolution optical spectroscopy. Using $\text{SFR}_{\text{H}\alpha}$ emission, they found that the western nucleus forms stars at a rate of $5 M_\odot \text{ yr}^{-1}$ while the eastern nucleus is quenched. The well-known dual AGN-host galaxy and merger remnant NGC 6240 shows an SFR of $100 M_\odot \text{ yr}^{-1}$ (Müller-Sánchez et al. 2018). Galaxy mergers or post-merger systems are found to show intense ongoing SFR. We have found similar results for our sample galaxies.

5.2 SFCs properties

We utilized the higher resolution UVIT images to probe star-forming regions in our sample galaxies. In the past few years, different studies have analyzed SFCs in nearby galaxies of different morphologies using UVIT observations to understand the SFC properties and distributions. Rahna et al. (2018) observed the barred spiral galaxy NGC 2336 with different filters of UVIT which is at a distance of 32.2 Mpc and has a size of $7.1 \times 3.9 \text{ arcmin}^2$. They detected 78 individual knots in NUV and 57 knots in FUV (which they call star-forming knots) with mean sizes of 485 and 408 pc in the FUV and NUV bands. Mondal, Subramaniam & George (2018) studied the nearby irregular dwarf galaxy WLM (distance: 995 kpc) with UVIT and detected several possible young stellar associations with 4–50 pc sizes. Yadav et al. (2021b) studied three nearby galaxies at distances varying between $\sim 6-7.5$ Mpc, with R_{25} ranging from 4.89 to 12 arcmin and a few hundreds of SFCs were detected with sizes ranging from a few parsecs to kpc and SFR density ranging from $\sim 10^{-3}$ to $10^{-1} M_\odot \text{ yr}^{-1} \text{ kpc}^{-2}$.

Most of these studies investigated the SFCs using UVIT in nearby large galaxies with very few galaxies around or beyond the distance of 70 Mpc. One such distant UVIT galaxy study is by Rakhi et al. (2023) where 56 knots with sizes ~ 1 to $\sim 35 \text{ Kpc}^2$ were detected

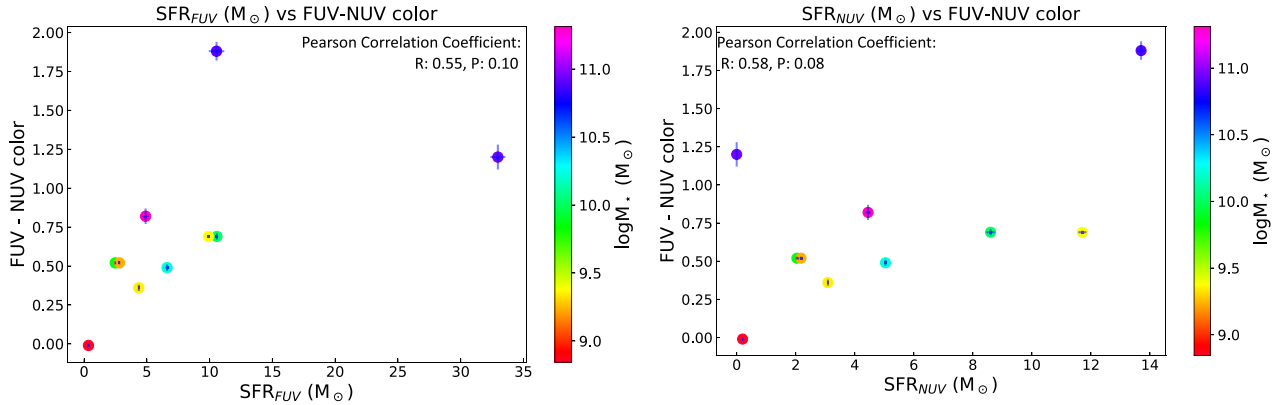


Figure 14. The correlations between FUV – NUV colour and SFR_{FUV} (left panel), SFR_{NUV} (right panel). These show a mild correlation.

in NGC 5291, which is at a distance of 62 Mpc. In our sample, while one galaxy, NGC 3773 is at a distance of ~ 18 Mpc it has a size of 40 arcsec, and SEXTRACTOR has detected only one SFC in the disc of the galaxy (Fig. 5). The remaining eight galaxies of our sample are situated at distances ranging from 73 to 293 Mpc and have a radius of ~ 20 –50 arcsec. We have detected 1–14 SFCs in FUV images and 1–19 SFCs in NUV images of our galaxies. There is no SFC detected only on the FUV image of SDSS J1436. The area size varies from 0.18 to 42 Kpc^2 . Most of the SFCs are situated in the disc. The calculated extinction corrected surface density (Σ_{SFR}) ranges from $\sim 0.0064 \pm 0.0004$ – $0.9069 \pm 0.0079 \text{ M}_{\odot} \text{ yr}^{-1} \text{ kpc}^{-2}$ (Table 7) which overlaps with Σ_{SFR} values of nearby spiral galaxies like NGC 628 (Yadav et al. 2021b).

5.3 FUV – NUV colour

The FUV – NUV colour maps can help us understand the stellar population in galaxies. Several UVIT studies of nearby galaxies have used the FUV – NUV colour to calculate the age of the resolved clumps. However, as we have sample galaxies that are small in size and are at large distances when we matched the resolution and created the colour maps, most of the clumps disappeared. Here, we have analyzed the colour maps with the radial profile of FUV – NUV colour (Figs 2–10). Gil de Paz et al. (2007) studied ~ 1136 galaxies in the *GALEX* field and examined their FUV – NUV colour. With an FUV – NUV colour range of ~ -0.20 to 3.0, they found a peak around (FUV – NUV) ~ 0.4 mag as well as a cut-off at (FUV – NUV) = 0.9 mag which separates elliptical/lenticular galaxies from spirals galaxies.

The total FUV – NUV colour is calculated using Galactic extinction corrected FUV and NUV magnitudes as given in Table 3 and it ranges from ~ 0 to 1.88 mag which is similar to that seen in other nearby galaxies (Boselli et al. 2005b; Boissier et al. 2018). The colour maps (lower left: Figs 2–10) show that all of our sample galaxies except one show a redder colour in the centre i.e. the FUV – NUV value is higher in the centre while the outskirts are relatively bluer (lower FUV – NUV value). NGC 3773 is the only galaxy that shows a bluer colour at the centre and has a redder ring around it (Fig. 5: lower left and middle panels). The variation of colour in our sample galaxies, from inwards to outwards implies the following (i) the central disc has more old stars than young stars, (ii) these galaxies are in a merger phase where the SF is happening predominantly in the outskirts, (iii) the dust attenuation varies throughout the galaxy. Our galaxies have high extinction and there is a spatial variation in

A_V of individual galaxies as seen from maximum and minimum A_V values (Table 4). However, with the present data, we cannot rule out other possibilities.

We checked whether any correlation exists between colour with stellar mass and FUV, NUV SFRs. The correlation between colour and the stellar mass is the same as the correlation between the A_V versus stellar mass (Fig. 11). The SFR_{FUV} , SFR_{NUV} are mildly correlated with colour with $R = 0.55$, $P = 0.10$ and $R = 0.58$, $P = 0.08$, respectively (Fig. 14).

We did notice that two of the AGN-hosted galaxies (viz., SDSS J1019, SDSS J1027) show extreme colour as well as extinction. However, these are the most distant as well as massive systems. Also, the other two AGN-hosted galaxies (MRK 739 and ESO509–IG066) show similar values to the star-forming galaxies. As our sample number is very small, we can not draw any strong conclusions on the active and non-active galaxies. We will explore it in the future.

The interacting galaxy, NGC4438 (Boselli et al. 2005a), shows a 20 kpc long tail, which is ~ 20 kpc away from the nucleus. Boselli et al. (2005a) found recent SF in tails and arms. However, most of the regions in the disc of the galaxy are dominated by old populations. Smith et al. (2010) studied the SF morphology and stellar population of 42 interacting systems in the nearby Universe. They found that tidal tails in the outskirts are bluer than the parent disc which can be due to enhanced SF due to interaction (Smith et al. 2010). The calculated FUV – NUV colour of our sample galaxies overlaps with the study by, for example, Gil de Paz et al. (2007) and Smith et al. (2010) as well as follows the same trend, i.e. redder disc and bluer outskirts. However, we could not perform the age analysis of spatially distributed SFCs (Mondal, Subramaniam & George 2018; Ujjwal et al. 2022). Hence, we can not rule out whether different stellar populations and/or dust attenuation are causing the colour variation.

5.4 Looking for AGN/stellar feedback

With three times better resolution than *GALEX*, UVIT shows resolved star-forming knots in a number of nearby galaxies. In Rubinur et al. (2021), one of our UVIT sample galaxies MRK 212 showed a pair of SFCs near the central AGN. This coincided with the radio emission having a flat spectral index. This could be a signature of AGN-jet-induced SF. In recent work, Nandi et al. (2023) detected three star-forming regions close to the nuclei of the AGN-hosted dwarf galaxy NGC 4395 which can be due to the AGN feedback effect. Joseph et al. (2022) detected star-forming sources in the direction of the radio jet of Centaurus A suggesting AGN feedback. George

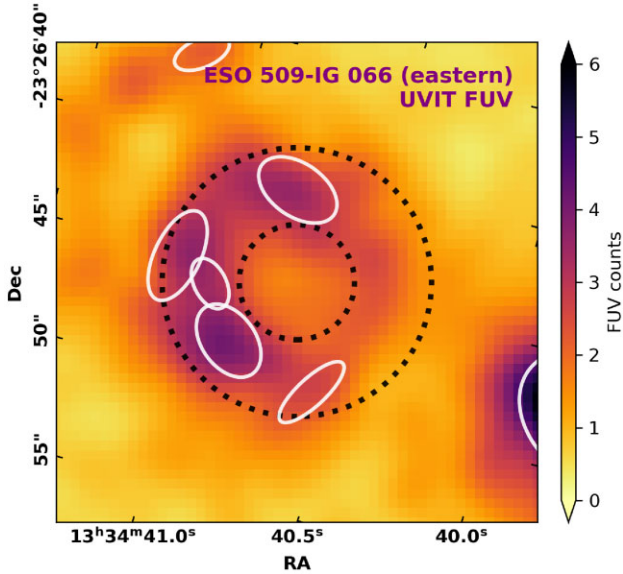


Figure 15. The FUV image of the eastern galaxy of ESO509–IG066-merger system. The white elliptical apertures are the SFCs, as shown in Fig. 7. The black-dotted ring is an artistic view: The SF is happening in a ring form which can be connected with central AGN which shows conical outflows. AGN may blow out the gas from the centre which gets compressed and cools down to form new stars in the ring.

et al. (2018a) have found signatures of the possible suppression of SF in NGC 7252 and explained it with possible AGN feedback. NGC 7252 shows red nuclei (Avg colour: ~ 1.0), followed by the inner bluer ring (Avg colour: ~ 0.45) and then the redder outer ring (Avg colour: ~ 1.4). This was explained as an AGN blowing out gas from the nuclear region which forms new stars in the inner blue ring (George et al. 2018a). Here, it should be noted that ring-like structures are present in many galaxies which are mainly the product of galaxy interactions, or stellar bars (Combes & Gerin 1985; Buta & Combes 1996).

We considered investigating feedback in our sample galaxies, although it is difficult as most of them are at a larger distance than the galaxies discussed above. Only in NGC 3773 which is ~ 18 Mpc away, we found a redder stellar ring around a blue nuclear emission. In NGC 3773, the radial profile shows a value close to zero (redder) at the centre and then it goes down to -0.2 (bluer) followed by rising to 0.6 (redder). Although we can not see any variation in the blue nuclei itself (and it is hard to explain 0 to -0.2) and there is a small difference in colour to draw any conclusions (unlike in NGC 7252), the blue nuclei and red ring may indicate that the centre has more recent SF considering the calculated extinction is very small in this galaxy. As previously mentioned, Linden et al. (2020) state that their sample including NGC 3773 is producing stars in the central 500 pc regions. A nuclear supernova or star cluster may be ionizing the gas and hence producing new stars that show a blue colour in the central region. Gao et al. (2023) explored the SF in the nearby dwarf galaxy-merger system NGC 4809/4810 where they found that the star-forming knots surrounded by the supernova show the highest SFR.

López-Cobá et al. (2020) have detected a cone-shaped [O III] outflow in the eastern nuclei of ESO509–IG066. Our FUV image shows UV deficiency in the same nucleus and SFCs distributed in a tentative ring surrounding the nucleus (Fig. 15). It is possible that outflowing materials is forming stars in the ring. The detailed study

of MRK 739 by Tubín et al. (2021) found that the eastern (left) nucleus is accreting as well as ionizing the northern regions and does not have much SF itself, whereas the western nucleus is not accreting but it falls in the star-forming main sequence. They proposed that this system is consistent with an early stage of the galaxy collision, where the foreground galaxy (W) is a young star-forming spiral galaxy in an ongoing first passage with its background companion elliptical galaxy (E). In this scenario, the eastern nucleus is ionizing one of the north-western spiral arms, similar to the ‘Hanny’s Voorwerps’ phenomena, as seen in IC 2497 (Sartori et al. 2016). We have detected SFCs (Fig. 6: SFC_{FUV} id 3, 7 and SFC_{NUV} id 5) in a similar position. This can be due to the AGN feedback process where the outflows associated with the eastern nucleus ionize the material and form stars in these SFCs.

6 SUMMARY AND CONCLUSIONS

We have studied the UVIT images from AstroSat of nine dual nuclei galaxies to understand SF in them. Below is the summary with the main findings:

(i) Our sample galaxies are chosen with separations below or around 10 kpc where eight galaxies have separation < 10 kpc and one system has a separation of 11 kpc. From MIR colour cut-offs, we checked whether AGN dominates the system and masked those nuclei.

(ii) The UVIT magnitudes match the *GALEX* magnitudes. The calculated magnitudes are corrected for both internal and external (Milky Way) extinctions.

(iii) The external extinction is calculated from the UV continuum slope (β). The β ranges from -2.03 ± 0.13 to 1.53 ± 0.01 . The total FUV extinction ranges from 0.53 ± 0.13 to 4.04 ± 0.01 and the NUV extinction ranges from 0.44 ± 0.10 to 3.10 ± 0.01 for the sample galaxies.

(iv) The extinction-corrected total FUV SFR ranges from 0.350 ± 0.002 to $32.96 \pm 0.62 M_{\odot} \text{ yr}^{-1}$ and total NUV SFR ranges from 0.203 ± 0.001 to $13.70 \pm 0.15 M_{\odot} \text{ yr}^{-1}$. The sSFR put all of our sample galaxies in a star-forming region in the sSFR– M_{\star} plane and it decreases with the increase of stellar mass.

(v) We have detected 1 to 14 SFCs in FUV images and 1 to 18 SFCs in NUV images. These SFCs are situated mostly in the disc and spiral arms.

(vi) The total FUV – NUV colour of the galaxies ranges from ~ 0 to 1.88. The colour maps of most of the galaxies show redder emission in nuclear regions and bluer in the outskirts. The one dwarf galaxy, NGC 3773 shows bluer nuclei and an outer redder ring. The colour variations in our sample galaxies can be either due to the dust variation or different stellar populations present which can be due to interactions.

(vii) The calculated extinction, SFR/sSFR, and colour values of our sample galaxies fall in the range of galaxy-merger systems from the literature. These quantities are correlated with stellar mass and no correlations are found between the SFR and the nuclear separation. However, it is difficult to draw any broad conclusion with a sample of nine galaxies.

(viii) We looked for any AGN or supernova-related feedback. The redder ring around the blue nuclei in the star-forming galaxy NGC 3773, the SFCs in a tentative ring-form around the east nuclei of dual AGN system ESO–IG066, or the SFCs on the spirals arm of MRK 739 indicate some signatures AGN/SNe feedback. However, we need to investigate further for confirmation with velocity information and/or finding the age of the populations, etc.

As our sample number is small and not homogeneous in terms of nuclear activity, stellar mass, or distance, we have avoided looking for any difference in active and non-active galaxies and this work is completely done to explore SF in dual nuclei galaxies. In the future, with a larger and more homogeneous sample, we will explore the correlations concerning nuclei types in detail.

ACKNOWLEDGEMENTS

We thank the referee for their comments which have improved the manuscript significantly. We acknowledge IIA, NCRA and UIO for providing the computational facilities. KR and PK acknowledge the support of the Department of Atomic Energy, Government of India, under project 12-R&D-TFR-5.02-0700. MD acknowledges the support of the Science and Engineering Research Board (SERB) Core research Grant CRG/2022/004531 for this research. This publication uses the data from the AstroSat mission of the Indian Space Research Organisation (ISRO), archived at the Indian Space Science Data Centre (ISSDC) which is a result of collaboration between IIA, Bengaluru, IUCAA, Pune, TIFR, Mumbai, several centres of ISRO, and CSA. The National Radio Astronomy Observatory is a facility of the National Science Foundation operated under a cooperative agreement by Associated Universities, Inc. This work has made use of the NASA ADS.⁷ This research has made use of the NASA/IPAC Extragalactic Database (NED), which is operated by the Jet Propulsion Laboratory, California Institute of Technology, under contract with the National Aeronautics and Space Administration. Funding for the Sloan Digital Sky Survey IV has been provided by the Alfred P. Sloan Foundation, the U.S. Department of Energy Office of Science, and the Participating Institutions. SDSS-IV acknowledges support and resources from the Center for High-Performance Computing at the University of Utah. The SDSS website is www.sdss.org. This publication makes use of data products from the Two Micron All Sky Survey, which is a joint project of the University of Massachusetts and the Infrared Processing and Analysis Center/California Institute of Technology, funded by the National Aeronautics and Space Administration and the National Science Foundation. RK thanks Prasanta Kumar Nayak for productive discussions.

DATA AVAILABILITY

The raw data can be obtained from the following data archive: (i) <https://astrobrowse.issdc.gov.in/astroarchive/archive/Home.jsp> (ii) <https://archive.nrao.edu/archive/advquery.jsp>

REFERENCES

- Bait O., Barway S., Wadadekar Y., 2017, *MNRAS*, 471, 2687
 Barnes J. E., Hernquist L., 1992, *ARA&A*, 30, 705
 Bertin E., Arnouts S., 1996, *A&AS*, 117, 393
 Bianchi L., 2011, *Ap&SS*, 335, 51
 Blecha L., Snyder G. F., Satyapal S., Ellison S. L., 2018, *MNRAS*, 478, 3056
 Boissier S., Cucciati O., Boselli A., Mei S., Ferrarese L., 2018, *A&A*, 611, A42
 Boselli A. et al., 2005a, *ApJ*, 623, L13
 Boselli A. et al., 2005b, *ApJ*, 629, L29
 Bournaud F., 2010, in Smith B., Higdon J., Higdon S., Bastian N. eds, ASP Conf. Ser. Vol. 423, *Galaxy Wars: Stellar Populations and Star Formation in Interacting Galaxies*. Astron. Soc. Pac., San Francisco. p. 177

- Brown M. J. I., Dey A., Jannuzi B. T., Brand K., Benson A. J., Brodwin M., Croton D. J., Eisenhardt P. R., 2007, *ApJ*, 654, 858
 Buat V., Takeuchi T. T., Burgarella D., Giovannoli E., Murata K. L., 2009, *A&A*, 507, 693
 Buta R., Combes F., 1996, *Fund. Cosmic Phys.*, 17, 95
 Calzetti D., 2013, *Secular Evolution of Galaxies*. Cambridge Univ. Press, Cambridge, p. 419
 Calzetti D., Armus L., Bohlin R. C., Kinney A. L., Koornneef J., Storchi-Bergmann T., 2000, *ApJ*, 533, 682
 Cluver M. E. et al., 2014, *ApJ*, 782, 90
 Combes F., Gerin M., 1985, *A&A*, 150, 327
 Cortese L., Gavazzi G., Boselli A., 2008, *MNRAS*, 390, 1282
 Daddi E. et al., 2007, *ApJ*, 670, 156
 Das M., Yadav J., Patra N., Dwarakanath K. S., McGaugh S. S., Schombert J., Rahna P. T., Murthy J., 2021, *JA&A*, 42, 85
 Elbaz D. et al., 2018, *A&A*, 616, A110
 Ellison S. L., Patton D. R., Simard L., McConnachie A. W., 2008, *AJ*, 135, 1877
 Ellison S. L., Patton D. R., Mendel J. T., Scudder J. M., 2011, *MNRAS*, 418, 2043
 Ellison S. L., Mendel J. T., Scudder J. M., Patton D. R., Palmer M. J. D., 2013, *MNRAS*, 430, 3128
 Ellison S. L. et al., 2022, *MNRAS*, 517, L92
 Fabian A. C., 2012, *ARA&A*, 50, 455
 Foord A., Gültekin K., Runnoe J. C., Koss M. J., 2021, *ApJ*, 907, 72
 Gaia Collaboration et al., 2023, *A&A*, 674, A1
 Gao Y., Gu Q., Liu G., Zhang H., Shi Y., Dou J., Li X., Kong X., 2023, *A&A*, 677, 13
 Ge J.-Q., Hu C., Wang J.-M., Bai J.-M., Zhang S., 2012, *ApJS*, 201, 31
 George K. et al., 2018a, *A&A*, 613, L9
 George K. et al., 2018b, *A&A*, 614, A130
 George K. et al., 2018c, *A&A*, 614, A130
 Gil de Paz A. et al., 2007, *ApJS*, 173, 185
 Gimeno G. N., Díaz R. J., Carranza G. J., 2004, *AJ*, 128, 62
 Goldader J. D., Meurer G., Heckman T. M., Seibert M., Sanders D. B., Calzetti D., Steidel C. C., 2002, *ApJ*, 568, 651
 Guainazzi M., Piconcelli E., Jiménez-Bailón E., Matt G., 2005, *A&A*, 429, L9
 Hao C.-N., Kennicutt R. C., Johnson B. D., Calzetti D., Dale D. A., Moustakas J., 2011, *ApJ*, 741, 124
 Harrison C. M., 2017, *Nat. Astron.*, 1, 0165
 Hopkins P. F., Hernquist L., 2009, *ApJ*, 694, 599
 Hopkins P. F., Quataert E., 2010, *MNRAS*, 407, 1529
 Hopkins P. F., Hernquist L., Cox T. J., Di Matteo T., Robertson B., Springel V., 2006, *ApJS*, 163, 1
 Hopkins P. F., Hernquist L., Cox T. J., Kereš D., 2008, *ApJS*, 175, 356
 Iglesias-Páramo J. et al., 2006, *ApJS*, 164, 38
 Ishibashi W., Fabian A. C., 2012, *MNRAS*, 427, 2998
 Jarrett T. H. et al., 2011, *ApJ*, 735, 112
 Joseph P., Sreekumar P., Stalin C. S., Paul K. T., Mondal C., George K., Mathew B., 2022, *MNRAS*, 516, 2300
 Kaviraj S., 2014, *MNRAS*, 437, L41
 Kennicutt Robert C. J., 1998, *ARA&A*, 36, 189
 Kennicutt Robert C. J., Keel W. C., van der Hulst J. M., Hummel E., Roettiger K. A., 1987, *AJ*, 93, 1011
 Knapen J. H., Cisternas M., Querejeta M., 2015, *MNRAS*, 454, 1742
 Koss M., Mushotzky R., Treister E., Veilleux S., Vasudevan R., Trippie M., 2012, *ApJ*, 746, L22
 Kumar A. et al., 2012, in *Proc. SPIE Conf. Ser. Vol. 8443, Space Telescopes and Instrumentation 2012: Ultraviolet to Gamma Ray*. SPIE, Bellingham. p. 84431N
 Linden S. T., Murphy E. J., Dong D., Momjian E., Kennicutt R. C. J., Meier D. S., Schinnerer E., Turner J. L., 2020, *ApJS*, 248, 25
 Liu X., Shen Y., Strauss M. A., Hao L., 2011, *ApJ*, 737, 101
 López-Cobá C. et al., 2020, *AJ*, 159, 167
 López-Sanjuan C., Balcells M., Pérez-González P. G., Barro G., García-Dabó C. E., Gallego J., Zamorano J., 2010, *ApJ*, 710, 1170

⁷<https://ui.adsabs.harvard.edu/>

- Mayer L., Kazantzidis S., Madau P., Colpi M., Quinn T., Wadsley J., 2007, *Science*, 316, 1874
- Mazzarella J. M., Gaume R. A., Aller H. D., Hughes P. A., 1988, *ApJ*, 333, 168
- Mazzarella J. M., Bothun G. D., Boroson T. A., 1991, *AJ*, 101, 2034
- Mazzarella J. M. et al., 2012, *AJ*, 144, 125
- Meurer G. R., Heckman T. M., Leitherer C., Kinney A., Robert C., Garnett D. R., 1995, *AJ*, 110, 2665
- Mezcua M., Lobanov A. P., Chavushyan V. H., León-Tavares J., 2011, *A&A*, 527, A38
- Mezcua M., Lobanov A. P., Mediavilla E., Karouzou M., 2014, *ApJ*, 784, 16
- Mihos J. C., Hernquist L., 1996, *ApJ*, 464, 641
- Mondal C., Subramaniam A., George K., 2018, *AJ*, 156, 109
- Moreno J. et al., 2019, *MNRAS*, 485, 1320
- Morganti R., 2017, *Frontiers Astron. Space Sci.*, 4, 42
- Müller-Sánchez F., Nevin R., Comerford J. M., Davies R. I., Privon G. C., Treister E., 2018, *Nature*, 556, 345
- Nandi P., Stalin C. S., Saikia D. J., Muneer S., Mountrichas G., Wylezalek D., Sagar R., Kissler-Patig M., 2023, *ApJ*, 950, 81
- Nordon R. et al., 2013, *ApJ*, 762, 125
- Pandey D., Saha K., Pradhan A. C., 2021, *ApJ*, 919, 101
- Pannella M. et al., 2015, *ApJ*, 807, 141
- Postma J. E., Leahy D., 2017, *PASP*, 129, 115002
- Rahna P. T., Das M., Murthy J., Gudennavar S. B., Bubbly S. G., 2018, *MNRAS*, 481, 1212
- Rakhi R. et al., 2023, *MNRAS*, 522, 1196
- Reddy N. A. et al., 2018, *ApJ*, 853, 56
- Rubinur K., Das M., Kharb P., 2019, *MNRAS*, 484, 4933
- Rubinur K., Kharb P., Das M., Rahna P. T., Honey M., Paswan A., Vaddi S., Murthy J., 2021, *MNRAS*, 500, 3908
- Rupke D. S. N., Veilleux S., 2011, *ApJ*, 729, L27
- Rupke D. S. N., Kewley L. J., Barnes J. E., 2010, *ApJ*, 710, L156
- Saitoh T. R., Daisaka H., Kokubo E., Makino J., Okamoto T., Tomisaka K., Wada K., Yoshida N., 2009, *Publ. Astron. Soc. Japan*, 61, 481
- Salim S. et al., 2007, *ApJS*, 173, 267
- Salim S. et al., 2016, *ApJS*, 227, 2
- Sartori L. F. et al., 2016, *MNRAS*, 457, 3629
- Schlafly E. F., Finkbeiner D. P., 2011, *ApJ*, 737, 103
- Schweizer F., 2005, in de Grijs R., González Delgado R. M. eds, *Astrophysics and Space Science Library* Vol. 329, *Starbursts: From 30 Doradus to Lyman Break Galaxies*. Kluwer, Dordrecht. p. 143
- Schweizer F., Seitzer P., Kelson D. D., Villanueva E. V., Walth G. L., 2013, *ApJ*, 773, 148
- Smith B. J., Giroux M. L., Struck C., Hancock M., 2010, *AJ*, 139, 1212
- Springel V., 2005, *MNRAS*, 364, 1105
- Stern D. et al., 2005, *ApJ*, 631, 163
- Stern D. et al., 2012, *ApJ*, 753, 30
- Tandon S. N. et al., 2020, *AJ*, 159, 158
- Tubín D. et al., 2021, *ApJ*, 911, 100
- Ujjwal K., Kartha S. S., Subramanian S., George K., Thomas R., Mathew B., 2022, *MNRAS*, 516, 2171
- Volonteri M., Haardt F., Madau P., 2003, *ApJ*, 582, 559
- Wright E. L. et al., 2010, *AJ*, 140, 1868
- Yadav J., Das M., Barway S., Combes F., 2021a, *A&A*, 651, L9
- Yadav J., Das M., Patra N. N., Dwarakanath K. S., Rahna P. T., McGaugh S. S., Schombert J., Murthy J., 2021b, *ApJ*, 914, 54
- Yadav J., Das M., Barway S., Combes F., 2023, *MNRAS*, 526, 198
- Yuan F. T., Takeuchi T. T., Matsuoka Y., Buat V., Burgarella D., Iglesias-Páramo J., 2012, *A&A*, 548, A117
- Zhang D., 2018, *Galaxies*, 6, 114

APPENDIX A: APPENDIX

Here, we present some additional images to support some of the analysis and arguments in the main text with proper references.

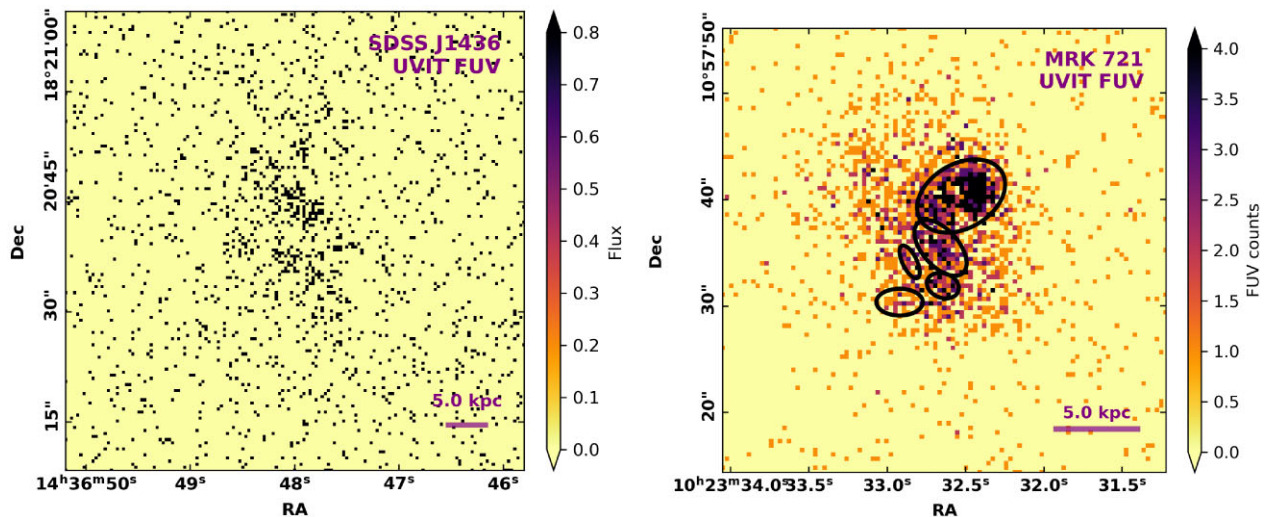


Figure A1. The unsmoothed UVIT images. Left-hand panel: the FUV image of SDSS J1436 where SEXTRACTOR could not detect any SFCs. Right-hand panel: the FUV image of MRK 721. The smoothed images may look like some of the SFCs do not look like convincing while other non-detected regions look like SFCs. However, it depends on the three-step criteria as mentioned in Section 4.2.1.

This paper has been typeset from a \LaTeX file prepared by the author.